Identification of new PTP1B-inhibiting decipiene diterpenoid esters from Eremophila clarkei by high-resolution PTP1B inhibition profiling, enzyme kinetics analysis, and molecular docking

Liang, Chao; Zang, Jie; Ndi, Chi; Semple, Susan; Buirchell, Bevan; Coriani, Sonia; Møller, Birger Lindberg; Stærk, Dan

Published in:
Bioorganic Chemistry

DOI:
10.1016/j.bioorg.2023.106744

Publication date:
2023

Document version
Publisher's PDF, also known as Version of record

Bioorganic Chemistry 139 (2023) 106744

Contents lists available at ScienceDirect

Bioorganic Chemistry

journal homepage: www.elsevier.com/locate/bioorg

Identification of new PTP1B-inhibiting decipiene diterpenoid esters from *Eremophila clarkei* by high-resolution PTP1B inhibition profiling, enzyme kinetics analysis, and molecular docking

Chao Liang [a], Jie Zang [a], Chi Ndi [b], Susan J. Semple [b], Bevan Buirchell [c], Sonia Coriani [d], Birger Lindberg Møller [e], Dan Staerk [a,*]

[a] *Department of Drug Design and Pharmacology, Faculty of Health and Medical Sciences, University of Copenhagen, Universitetsparken 2, DK-2100 Copenhagen, Denmark*
[b] *Quality Use of Medicines and Pharmacy Research Centre, Clinical and Health Sciences, University of South Australia, Frome Road, Adelaide 5000, Australia*
[c] *Wise Owl Consulting, Como, Western Australia 6152, Australia*
[d] *Department of Chemistry, Technical University of Denmark, Kemitorvet Building 207, DK-2800 Kongens Lyngby, Denmark*
[e] *Plant Biochemistry Laboratory, Department of Plant and Environmental Sciences, University of Copenhagen, Thorvaldsensvej 40, DK-1871 Frederiksberg C, Denmark*

ARTICLE INFO

Keywords:
Eremophila clarkei
Decipiene diterpenoids
PTP1B inhibitory activity
High-resolution inhibition profiling
Enzyme kinetics
Molecular docking

ABSTRACT

In this study, an extract of the leaves of *Eremophila clarkei* Oldfield & F.Muell. showed protein tyrosine phosphatase 1B (PTP1B) inhibitory activity with an IC_{50} value of 33.0 μg/mL. The extract was therefore investigated by high-resolution PTP1B inhibition profiling to pinpoint the constituents responsible for the activity. Subsequent isolation and purification using analytical-scale HPLC led to identification of eight previously undescribed decipiene diterpenoids, eremoclarkanes A-H, as well as eremoclarkic acid, a biogenetically related new phenolic acid. In addition, one known decipiene diterpenoid and ten known *O*-methylated flavonoids were isolated. The structures of the isolated compounds were elucidated by extensive analysis of their HRMS and 1D and 2D NMR spectra. The absolute configuration of decipiene diterpenoids was determined by comparison of experimental and calculated ECD spectra. The flavonoid hispidulin (**2b**) and the four decipiene diterpenoids **13a**, **13b**, **13f**, and **14b** exhibited PTP1B inhibitory activity with IC_{50} values ranging from 22.8 to 33.6 μM. This is the first report of PTP1B inhibitory activity of decipienes, and enzyme kinetics revealed that **13a** and **13b** are competitive inhibitors of PTP1B, whereas **13f** and **14b** displayed mixed-type-mode inhibition of PTP1B. Finally, molecular docking indicated that **13a**, **13b**, **13f**, and **14b** showed comparable binding affinity towards the active and/or allosteric site of PTP1B enzyme. Structure-activity relationship (SAR) of the identified *O*-methylated flavonoids and decipiene diterpenoids towards PTP1B is discussed. Plausible enzymatic and photochemically driven routes for the formation of the decipienes and conversion products thereof are presented and discussed.

1. Introduction

Plants of the genus *Eremophila* (Scrophulariaceae) are endemic to Australia and mainly distributed in the arid and semi-arid regions of Australia. *Eremophila* consists of approximately 230 species, of which some have been used in traditional Australian Aboriginal medicine [1]. *Eremophila* is rich in structurally diverse and unique diterpenoids, with serrulatane, decipiene, viscidane, cembrene, and eremane type diterpenoids being most abundant [2]. A range of pharmacological properties have been reported for *Eremophila* diterpenoids, including antibacterial [3–7], anti-inflammatory [7], antidiabetic [8–10], and cytotoxic activity [6]. *Eremophila clarkei* Oldfield & F.Muell., is an erect shrub widespread in West and South Australia, and also found in the extreme south western region of the Northern Territory [1,11]. In a previous study, the identification of cembrene diterpenoids in *E. clarkei* was reported [12], but no pharmacological studies of this species have been reported.

Type 2 diabetes (T2D), which accounts for 90–95% of all diabetes cases [13], is characterized by chronic hyperglycaemia and is mainly caused by a lowered response to insulin (insulin resistance) and/or an inadequate insulin secretion by the β-pancreatic cells [14,15]. Protein tyrosine phosphatases are a large family of enzymes playing an important role in cellular signaling by regulating the phosphorylation of target

* Corresponding author.
E-mail address: ds@sund.ku.dk (D. Staerk).

https://doi.org/10.1016/j.bioorg.2023.106744
Received 21 April 2023; Received in revised form 3 July 2023; Accepted 17 July 2023
Available online 20 July 2023

proteins [16]. Protein tyrosine phosphatase 1B (PTP1B) is considered a promising T2D target due to its function as a negative regulator of the insulin response. In the insulin signaling pathway, PTP1B dephosphorylates the insulin receptor and insulin receptor substrate, which results in decreased insulin sensitivity [17]. Even though a large number of PTP1B inhibitors have been reported, either from natural sources or through synthesis, no clinically approved drugs targeting PTP1B are available. The major challenges for development of PTP1B inhibitors as T2D drugs seem to be associated with selectivity and bioavailability [18,19].

Natural product-based drug discovery is strongly dependent on analytical techniques to pinpoint bioactive constituents in complex extracts, and high-resolution inhibition profiling has proven successful for this purpose. Thus, the eluate from analytical-scale HPLC is microfractionated into one or more 96-well microplates, followed by *in vitro* assaying of the dried contents in each well. The bioactivity of each well, calculated as percentage inhibition, is plotted against the corresponding retention time, and visually presented in the form of a high-resolution inhibition profile overlaid with UV and/or MS traces from the HPLC separation. This allows easy pinpointing of chromatographic peaks correlated with *in vitro* bioactivity. When combined with e.g., HPLC-PDA-HRMS or HPLC-PDA-HRMS-SPE-NMR analysis, the time used for structural identification of bioactive constituents in complex extracts is dramatically reduced. This bioanalytical platform has been successfully used for accelerated identification of different classes of α-glucosidase inhibitors [9,10,20–22,24], α-amylase inhibitors [22,23], aldose reductase inhibitors [24], PTP1B inhibitors [8–10,20–22,25], and DPP-IV inhibitors [26] from complex plant extracts.

In the present study, high-resolution PTP1B inhibition profiling combined with HPLC-PDA-HRMS and NMR spectroscopy were applied for identification of PTP1B inhibitors in *E. clarkei*. Eight previously undescribed and one known decipiene diterpenoids, one biogenetically related new phenolic acid, as well as ten known *O*-methylated flavonoids were identified. Among all these compounds, the flavonoid hispidulin and four new decipiene diterpenoids exhibited promising PTP1B inhibitory activity. This is the first study reporting PTP1B inhibitory activity of decipiene diterpenoids. Structure-activity relationship (SAR) of all tested compounds are discussed. Plausible enzymatic as well as photochemically driven steps involved in decipiene metabolism are presented.

2. Experimental section

2.1. General experimental procedures

Analytical-scale HPLC experiments were conducted using an Agilent 1200 series instrument (Agilent Technologies, Santa Clara, CA, USA) consisting of a G1367C high-performance autosampler, a G1311A quaternary pump, a G1322A degasser, a G1316A thermostatted column compartment, a G1315C photodiode array detector, and a G1364C fraction collector, all controlled by Agilent ChemStation version B.03.02 software. A flow rate of 0.5 mL/min and a temperature of 40 °C were maintained for all experiments. HPLC-PDA-HRMS experiments were performed using an Agilent 1260 HPLC system (Agilent Technologies, Santa Clara, CA, USA) consisting of a G1311B quaternary pump with a built-in degasser, a G1329B autosampler, a G1316A thermostatted column compartment, and a G1315D photodiode array detector, coupled with a Bruker micrOTOF-Q II mass spectrometer (Bruker Daltonik, Bremen, Germany) equipped with an electrospray ionization source. NMR experiments were performed at 300 K using a Bruker Avance III system (^{1}H and ^{13}C operating frequency of 600.13 and 150.90 MHz, respectively) equipped with a Bruker SampleJet and a cryogenically cooled gradient inverse triple-resonance 1.7 mm TCI probe-head (Bruker Biospin, Karlsruhe, Germany). Experimental ECD spectra were recorded using a JASCO J-1500 CD spectrometer (JASCO, Tokyo, Japan).

2.2. Chemicals and reagents

α-Glucosidase type I (EC 3.2.1.20, from *Saccharomyces cerevisiae*, lyophilized powder), α-amylase type VI-B (E.C. 3.2.1.1, from porcine pancreas, lyophilized powder), $NaH_2PO_4{\cdot}2H_2O$, Na_2HPO_4, NaN_3, NaOH, NaCl, calcium acetate, 2-chloro-4-nitrophenyl-α-D-maltotrioside (CNP-G3), *p*-nitrophenyl α-D-glucopyranoside (*p*-NPG), *p*-nitrophenyl phosphate (*p*-NPP), dimethyl sulfoxide (DMSO), tris(hydroxymethyl)-aminomethane (Tris), bis(2-hydroxyethyl)-imino-tris(hydroxymethy lmethane) (Bis-Tris), *N,N,N′,N′*-ethylenediaminetetraacetate (EDTA), dithiothreitol (DTT), phosphoric acid and acetic acid were purchased from Sigma-Aldrich (St. Louis, MO, USA) and recombinant human protein tyrosine phosphatase 1B (PTP1B) (BML-SE332-0050, EC 3.1.3.48) from Enzo Life Sciences (Farmingdale, NY, USA). Methanol-d_4 was purchased from Euriso-top (Saint-Aubin Cesex, France), formic acid from Merck (Darmstadt, Germany). Acetonitrile and methanol were HPLC grade from VWR International (Søborg, Denmark). Purification of water was performed by deionization and filtration through a 0.22-μm membrane on a Milli-Q Plus system (Millipore, Billerica, MA, USA).

2.3. Plant material

Leaves of *Eremophila clarkei* were collected on the Summit Walk, Kennedy Range National Park, Western Australia (24 40 19 S; 115 10 09 E) in July 2017. A voucher specimen was lodged at the University of Melbourne Herbarium, Melbourne, Victoria, Australia (accession number MELUD127857a).

2.4. Extraction

To extract leaf resins, leaf material (18.19 g) was submerged in 200 mL of acetonitrile and shaken for 10 min (Ratek, Knox City, Victoria, Australia). The extract was filtered using a glass funnel and dried *in vacuo* at 40 °C using a rotary evaporator (IKA RV10). The dry extract (2.37 g) was transferred to amber-colored vials using a small volume of methanol and dried under nitrogen gas, then stored at −20 °C.

2.5. PTP1B inhibition assay

The PTP1B inhibition assay was performed as described before [20]. In short, the test substance in each well of a 96-well microplate was dissolved in 18 μL of DMSO, and diluted to a total volume of 180 μL by adding 52 μL of EDTA solution (3.4 mM in buffer), and 60 μL of substrate solution (1.5 mM *p*-NPP and 6 mM DTT in buffer). The buffer was prepared by mixing 50 mM Tris, 50 mM Bis-Tris and 100 mM NaCl in Milli-Q water, followed by adjustment of pH value to 7.0 with acetic acid. The microplate was incubated at 25 °C for 10 min before initiation of enzymatic reaction by adding 50 μL of 0.001 μg/μL PTP1B stock solution to each well. The absorbance of cleavage product *p*-nitrophenol produced in each well was measured at 405 nm every 30 s for 10 min to obtain the enzyme activity expressed as ΔAU/min. A Thermo Scientific Multiskan FC microplate reader (Thermo Scientific, Waltham, MA, USA) with a built-in incubator was used for incubation and absorbance measurement, controlled by SkanIt ver. 2.5.1 software. DMSO was used as a blank sample and RK-682 as a reference compound. All measurements were performed in triplicate. The PTP1B inhibition was calculated using equation 1:

$$\text{Percent inhibition} = \frac{\text{Slope(blank)} - \text{Slope(sample)}}{\text{Slope(blank)}} \times 100\% \quad (1)$$

2.6. α-Glucosidase inhibition assay

The α-glucosidase inhibition assay was performed as described before [20]. In short, the test substance was dissolved in 10 μL of DMSO in each well of a 96-well microplate, and 90 μL buffer and 80 μL

α-glucosidase enzyme solution (2.0 U/mL in buffer) was added. The buffer was prepared by mixing 34 mM $NaH_2PO_4{\cdot}2H_2O$, 66 mM Na_2HPO_4 and 0.02% NaN_3 in Milli-Q water, followed by adjustment of pH value to 7.5 with NaOH. The microplate was incubated at 28 °C for 10 min before initiating the enzymatic reaction by adding 20 μL *p*-NPG solution (10 mM in buffer) to give a total volume of 200 μL in each well. The absorbance was measured at 405 nm every 30 *sec* for 35 min to obtain the enzyme activity expressed as ΔAU/s. The above-mentioned microplate reader was used for incubation and absorbance measurement, and all measurements were performed in triplicates. Percentage α-glucosidase inhibition was calculated using the same equation as for the PTP1B inhibition assay.

2.7. α-Amylase inhibition assay

The α-amylase inhibition assay was performed as described before [22]. Similar to the procedure of the α-glucosidase inhibition assay, the test substance was dissolved in 20 μL of DMSO in each well of a 96-well microplate, and diluted in 80 μL buffer and 80 μL α-amylase enzyme solution (2.0 U/mL in buffer). The buffer (0.1 M) was prepared by mixing $NaH_2PO_4{\cdot}2H_2O$, Na_2HPO_4, 60 mM NaCl and 0.02% NaN_3 in Milli-Q water, followed by adjustment of pH value to 6.0 with phosphoric acid and addition of 1 mM calcium acetate. The microplate was incubated at 37 °C for 10 min before initiation of enzymatic reaction by adding 20 μL CNP-G3 solution (10 mM in buffer) to give a total volume of 200 μL in each well. The absorbance was measured at 405 nm every 3 min for 30 min on the above-mentioned microplate reader. All measurements were performed in triplicate. Percentage α-amylase inhibition was calculated using the same equation described before.

2.8. Microfractionation and high-resolution PTP1B inhibition profiling

The acetonitrile extract of *E. clarkei* was microfractionated using the above-mentioned Agilent 1200 analytical-scale HPLC. The flow rate was 0.5 mL/min and the temperature was maintained at 40 °C. The mobile phase for the HPLC separation was a mixture of solvent A (acetonitrile–water-formic acid, 5:94.9:0.1, v/v/v) and solvent B (acetonitrile–water-formic acid, 94.9:5:0.1, v/v/v). For the high-resolution PTP1B inhibition profiling, 10 μL acetonitrile solution of crude leaf extract (50 mg/mL) was separated on a reversed-phase Phenomenex Luna C_{18}(2) column (150 × 4.6 mm i.d., 3 μm particle size, 100 Å pore size) based on the following gradient: 0 min, 25% B; 30 min 100% B; 38 min, 100% B; 39 min, 25% B; 46 min, 25% B. The eluate from 5 to 35 min was fractionated into 88 wells of one 96-well microplate (resolution of 2.93 data points per minute), and the sampled eluate was evaporated to dryness using a Savant SPD121P speed vacuum concentrator equipped with an OFP400 oil-free pump and an RVT400 refrigerated vapor trap (Holbrook, NY, USA). The dried material in the microplate was subsequently assayed for PTP1B inhibitory activity, providing the percentage inhibition of each well, which was plotted against the corresponding retention time of the HPLC chromatogram to create the high-resolution PTP1B inhibition profile.

2.9. Dose-dependent effect determination

Dose-dependent effects of PTP1B inhibition were determined according to the procedure described above. Test substances were dissolved in DMSO and two-fold serial dilutions for this stock solution were assayed for PTP1B inhibitory activity. The dilution series started from 2 mg mL^{-1} and 2 mM for the crude extract and pure compounds, respectively, and all measurements were performed in triplicate. IC_{50} values were calculated on the basis of equation 2 below using GraFit software, version 5.0.11 (Erithacus Software Limited):

$$f(x) = \min + \frac{\max - \min}{1 + \left(\frac{x}{IC_{50}}\right)^{slope}} \quad (2)$$

where min is the minimum and max the maximum concentrations, x is the concentration of the test sample and slope is the Hill slope. Results were expressed as IC_{50} mean value ± standard error.

2.10. Analytical-scale HPLC separations

A total of 130 successive 20-μL injections of acetonitrile leaf extract of *E. clarkei* (50 mg/mL) were separated on the above-mentioned 1200 series Agilent HPLC instrument using the same elution solvents, gradient, column, flow rate, and temperature as described in Section 2.8. Automated UV threshold-based collection resulted in isolation of pure **1** (1.80 mg), **3** (0.72 mg), **4** (2.14 mg), **5** (1.44 mg), **6** (1.70 mg), **7** (1.30 mg), **8** (1.42 mg), **9** (1.01 mg), **10** (2.51 mg), and **12** (3.20 mg) as well as fractions *2* (2.50 mg), *11* (12.58 mg), *13* (8.08 mg), and *14* (2.12 mg).

Fractions *13* and *14* were reseparated using the same analytical-scale C_{18} column, whereas fractions *2*, *11* and '*13c-13e*' were further purified on a Phenomenex Kinetex PFP column (150 × 4.6 mm i.d., 2.6 μm particle size, 100 Å pore size), using a mobile phase consisting of solvent A (methanol–water-formic acid, 5:94.9:0.1, v/v/v) and solvent B (methanol–water-formic acid, 94.9:5:0.1, v/v/v). The material eluted with fraction *2* was purified by 25 successive separations of 10-μL injections (10.0 mg/mL in methanol) using the following elution gradient: 0 min, 50% B; 15 min, 100% B; 18 min, 100% B; 19 min, 50% B; 25 min, 50% B; the material eluted with fraction *11* by 64 successive separations of 10-μL injections (26.1 mg/mL in methanol) using the following elution gradient: 0 min, 55% B; 20 min, 100% B; 25 min, 100% B; 26 min, 55 %B; 32 min, 55% B; the material eluted with fraction '*13c-13e*' by 25 successive separations of 8-μL injections (8.3 mg/mL in methanol) using the following elution gradient: 0 min, 80% B; 6 min, 88% B; 11 min, 91% B; 13 min, 100% B; 17 min, 100% B; 18 min, 80 %B; 24 min, 80% B; the material eluted with fraction *13* by 82 successive separations of 5-μL injections (13.5 mg/mL in methanol) using the following elution gradient: 0 min, 65% B; 8 min, 84% B; 16 min, 92% B; 20 min, 100% B; 25 min, 100% B; 26 min, 65 %B; 32 min, 65% B; and finally the material eluted with fraction *14* by 29 successive separations of 10-μL injections (7.1 mg/mL in methanol) using the following elution gradient: 0 min, 80% B; 20 min, 100% B; 25 min, 100% B; 26 min, 80 %B; 32 min, 80% B. This resulted in isolation of pure **2a** (0.67 mg), **2b** (0.80 mg), **11a** (8.30 mg), **11b** (3.20 mg), **13a** (0.70 mg), **13b** (1.40 mg), **13c** (0.42 mg), **13d** (0.24 mg), **13e** (0.81 mg), **13f** (0.96 mg), **14a** (0.05 mg), **14b** (0.37 mg), and **14c** (0.13 mg) (Figs. S2-S6).

Eremoclarkane A ***(1)****:* white amorphous solid; see Table 2 for ^1H (600 MHz) and ^{13}C NMR (150 MHz) spectroscopic data; HRESIMS (negative mode) *m/z* 351.2168 $[M-H]^-$ (calcd for $C_{20}H_{31}O_5^-$ 351.2177, ΔM +2.6 ppm).

Eremoclarkic acid ***(2a)****:* white amorphous solid; see Table 2 for ^1H (600 MHz) and ^{13}C NMR (150 MHz) spectroscopic data; HRESIMS (negative mode) *m/z* 349.2018 $[M-H]^-$ (calcd for $C_{20}H_{29}O_5^-$ 349.2020, ΔM +0.7 ppm).

Eremoclarkane B ***(10)****:* white amorphous solid; see Table 2 for ^1H (600 MHz) and ^{13}C NMR (150 MHz) spectroscopic data; HRESIMS

Table 1
Inhibitory activity of acetonitrile extract of *E. clarkei* against PTP1B, α-glucosidase and α-amylase.

Enzyme	Inhibition at 50 μg/mL (%)[a]	IC_{50} (μg/mL)[a]
PTP1B	82.2 ± 2.8	33.0 ± 0.8
α-glucosidase	3.2 ± 0.8	–
α-amylase	1.0 ± 0.4	–

[a] Results presented as mean value ± standard error of three independent experiments.

Table 2
^{1}H NMR (600 MHz) and ^{13}C NMR (150 MHz) spectroscopic data of **1**, **2a** and **10** in methanol-d_4 (δ in ppm, J in Hz).

Position	**1**		**2a**		**10**	
	δ_C, type[a]	δ_H, mult (J)[b]	δ_C, type[a]	δ_H, mult (J)[b]	δ_C, type	δ_H, mult (J)[b]
1	30.5, CH	1.65, m[c]	33.2, CH	3.22, tq (7.6, 7.0)	30.2, CH	1.64, m[c]
2	27.8, CH_2	α: 1.33, m[c] β: 1.66, m[c]	37.7, CH_2	A: 1.62, m B: 1.73, m	26.9, CH_2	α: 1.30, m[c] β: 1.60, m[c]
3	21.4, CH_2	α: 1.50, m[c] β: 1.22, m[c]	26.5, CH_2	1.97, m[c]	20.8, CH_2	1.50, m
4	35.5, CH	1.95, ddd (12.5, 10.0, 7.0)	127.2, CH	5.41, t (7.2)	35.1, CH	2.10, q (9.6)
5	38.2, CH	3.11, d (9.0)	121.9, CH	7.45, br d (7.8)	38.2, CH	3.13, d (9.6)
6	132.9, C	–	131.1, C	–	131.9, C	–
7	142.8, CH	6.88, br d (1.2)	116.8, CH	7.41, br s	140.8, CH	7.19, br dd (6.4, 1.8)
8	67.4, CH	4.22, br dd (7.2, 1.2)	155.6, C	–	26.6, CH_2	α: 2.05, m[c] β: 2.41, m
9	39.9, CH	1.48, m[c]	139.6, C	–	30.1, CH	1.58, m[c]
10	31.9, CH	2.82, q (9.4)	127.6, CH	7.18, br d (7.8)	31.7, CH	2.72, q (9.6)
11	48.4, C	–	140.0, C	–	48.5, C	–
12	28.2, CH_2	1.26, m[c]	28.7, CH_2	1.97, m[c]	27.8, CH_2	1.31, m[c]
13	22.7, CH_2	A: 0.98, m[c] B: 1.27, m[c]	26.7, CH_2	A: 1.31, m[c] B: 1.39, m[c]	23.7, CH_2	A: 1.74, m B: 1.92, m
14	35.0, CH_2	A: 0.97, m[c] B: 1.28, m[c]	34.1, CH	A: 1.01, m B: 1.34, m[c]	127.1, CH	5.30, t (7.0)
15	36.4, CH	1.51, m[c]	36.4, CH	1.52, m	135.1, C	–
16	68.1, CH_2	A: 3.26, dd (10.6, 6.7) B: 3.36, dd (10.6, 5.9)	68.1, CH_2	A: 3.28, dd (10.6, 6.7)[d] B: 3.38, dd (10.6, 5.8)	68.7, CH_2	3.87, s
17	16.8, CH_3	0.85, d (6.7)	16.8, CH_3	0.86, d (6.7)	13.5, CH_3	1.60, s
18	69.6, CH_2	A: 3.64, d (10.8) B: 3.70, d (10.8)	67.0, CH_2	3.93, br s	70.1, CH_2	A: 3.69, d (10.7) B: 3.75, d (10.7)
19	171.8, C	–	170.9, C	–	171.8, C	–
20	21.6, CH_3	1.13, d (6.5)	21.0, CH_3	1.22, d (7.0)	20.3, CH_3	0.98, d (6.6)

[a] ^{13}C NMR data assigned by HSQC and HMBC experiments.
[b] Multiplicities reported as apparent splittings: s = singlet, d = doublet, t = triplet, q = quartet, m = multiplet, br = broad.
[c] Multiplicities undetermined due to overlapping signals.
[d] Overlapped with solvent signal.

(negative mode) m/z 333.2067 $[M-H]^-$ (calcd for $C_{20}H_{29}O_4^-$ 333.2071, ΔM +1.3 ppm).

Eremoclarkane C ***(13a)****:* white amorphous solid; see Table 3 for ^{1}H (600 MHz) and ^{13}C NMR (150 MHz) spectroscopic data; HRESIMS (negative mode) m/z 479.2418 $[M-H]^-$ (calcd for $C_{29}H_{35}O_6^-$ 479.2439, ΔM +4.4 ppm).

Eremoclarkane D ***(13b)****:* white amorphous solid; see Table 3 for ^{1}H

Table 3
^{1}H NMR (600 MHz) and ^{13}C NMR (150 MHz) spectroscopic data of **13a**, **13b** and **13c** in methanol-d_4 (δ in ppm, J in Hz).

Position	**13a**		**13b**		**13c**	
	δ_C, type[a]	δ_H, mult (J)[b]	δ_C, type	δ_H, mult (J)[b]	δ_C, type[a]	δ_H, mult (J)[b]
1	30.2, CH	1.62, m[c]	30.2, CH	1.62, m[c]	30.2, CH	1.62, m[c]
2	26.9, CH_2	α: 1.59, m[c] β: 1.30, m[c]	26.9, CH_2	α: 1.56, m[c] β: 1.26, m[c]	26.8, CH_2	α: 1.58, m[c] β: 1.30, m[c]
3	20.8, CH_2	1.50, m	20.7, CH_2	1.45, m	20.7, CH_2	1.46, m
4	35.1, CH	2.08, m[c]	35.1, CH	2.05, m[c]	35.1, CH	2.06, m[c]
5	38.2, CH	3.13, d (9.4)	38.0, CH	3.12, d (9.4)	38.2, CH	3.12, d (9.6)
6	132.3, C	–	132.0, C	–	132.3, C	–
7	140.2, CH	7.17, br d (6.4)	140.7, CH	7.18, br d (4.8)	140.0, CH	7.16, br dd (6.4, 1.8)
8	26.6, CH_2	α: 2.06, m[c] β: 2.40, m	26.5, CH_2	α: 2.04, m[c] β: 2.38, m	26.5, CH_2	α: 2.06, m[c] β: 2.41, m
9	30.1, CH	1.58, m[c]	30.1, CH	1.56, m[c]	30.1, CH	1.58, m[c]
10	31.7, CH	2.72, q (9.4)	31.6, CH	2.70, q (9.4)	31.6, CH	2.71, q (9.4)
11	48.5, C	–	48.6, C	–	48.5, C	–
12	27.3, CH_2	1.33, m[c]	28.1, CH_2	1.26, m[c]	28.0, CH_2	A: 1.22, m[c] B: 1.28, m[c]
13	23.9, CH_2	A: 1.78, m B: 1.96, m	22.7, CH_2	A: 1.03, m B: 1.26, m[c]	22.4, CH_2	A: 1.07, m[c] B: 1.19, m[c]
14	130.7, CH	5.42, t (7.0)	35.3, CH_2	A: 1.12, m B: 1.32, m[c]	35.0, CH_2	A: 1.06, m[c] B: 1.28, m[c]
15	130.8, C	–	33.7, CH	1.78, m	33.4, CH	1.71, m
16	70.8, CH_2	4.53, s	69.9, CH_2	3.98, m	70.2, CH_2	A: 3.81, dd (10.7, 6.7) B: 3.90, dd (10.7, 6.0)
17	13.8, CH_3	1.65, s	17.2, CH_3	0.94, (6.6)	16.8, CH_3	0.88, d (6.7)
18	70.1, CH_2	A: 3.70, d (10.7) B: 3.75, d (10.7)	70.1, CH_2	A: 3.66, d (10.7) B: 3.71, d (10.7)	70.2, CH_2	A: 3.65, d (10.7) B: 3.72, d (10.7)
19	172.3, C	–	171.7, C	–	172.2, C	–
20	20.3, CH_3	0.98, d (6.6)	20.2, CH_3	0.95, d (6.6)	20.3, CH_3	0.98, d (6.7)
1′	169.0, C	–	169.1, C	–	172.9, C	–
2′	114.9, CH	6.32, d (15.9)	115.0, CH	6.31, d (15.9)	20.5, CH_3	2.02, s
3′	146.2, CH	7.60, d (15.9)	146.2, CH	7.60, d (15.9)		
4′	126.9, C	–	126.9, C	–		
5′	130.9, CH	7.46, d (8.6)	130.9, CH	7.46, d (8.6)		
6′	116.6, CH	6.81, d (8.6)	116.6, CH	6.81, d (8.6)		
7′	161.0, C	–	161.0, C	–		
8′	116.6, CH	6.81, d (8.6)	116.6, CH	6.81, d (8.6)		

(*continued on next page*)

Table 3 (*continued*)

Position	**13a**		**13b**		**13c**	
	δ_C, type[a]	δ_H, mult (J)[b]	δ_C, type	δ_H, mult (J)[b]	δ_C, type[a]	δ_H, mult (J)[b]
9′	130.9, CH	7.46, d (8.6)	130.9, CH	7.46, d (8.6)		

[a] ^{13}C NMR data assigned by HSQC and HMBC experiments.
[b] Multiplicities reported as apparent splittings: s = singlet, d = doublet, t = triplet, q = quartet, m = multiplet, br = broad.
[c] Multiplicities undetermined due to overlapping signals.

(600 MHz) and ^{13}C NMR (150 MHz) spectroscopic data; HRESIMS (negative mode) *m/z* 481.2579 $[M-H]^-$ (calcd for $C_{29}H_{37}O_6^-$ 481.2596, ΔM +3.5 ppm).

Eremoclarkane E ***(13c)****:* white amorphous solid; see Table 3 for ^{1}H (600 MHz) and ^{13}C NMR (150 MHz) spectroscopic data; HRESIMS (negative mode) *m/z* 377.2316 $[M-H]^-$ (calcd for $C_{22}H_{33}O_5^-$ 377.2333, ΔM +4.6 ppm).

Eremoclarkane F ***(13d)****:* white amorphous solid; see Table 4 for ^{1}H (600 MHz) and ^{13}C NMR (150 MHz) spectroscopic data; HRESIMS (negative mode) *m/z* 481.2586 $[M-H]^-$ (calcd for $C_{29}H_{37}O_6^-$ 481.2596, ΔM +2.0 ppm).

Eremoclarkane G ***(13f)****:* white amorphous solid; see Table 4 for ^{1}H (600 MHz) and ^{13}C NMR (150 MHz) spectroscopic data; HRESIMS (negative mode) *m/z* 511.2680 $[M-H]^-$ (calcd for $C_{30}H_{39}O_7^-$ 511.2701, ΔM +4.2 ppm).

Eremoclarkane H ***(14b)****:* white amorphous solid; see Table 4 for ^{1}H (600 MHz) and ^{13}C NMR (150 MHz) spectroscopic data; HRESIMS (negative mode) *m/z* 465.2626 $[M-H]^-$ (calcd for $C_{29}H_{37}O_5^-$ 465.2646, ΔM +4.4 ppm).

2.11. HPLC-PDA-HRMS experiments

High-resolution MS data were acquired in negative-ion mode with a capillary voltage of 3500 V, a drying temperature of 200 °C, a nebulizer pressure of 2.0 bar and a drying gas flow of 7 L/min. A solution of sodium formate clusters was injected at the beginning of the analysis to enable internal mass calibration. Chromatographic separations were conducted using the same column and conditions as used for the analytical-scale HPLC separation.

2.12. NMR experiments

NMR data of all isolated compounds were acquired at 300 K in methanol-d_4, and the residual solvent signals (δ_H 3.31 ppm and δ_C 49.0 ppm) were used for chemical shift calibration. ^{1}H NMR spectra were recorded with 30° pulses, acquisition time of 2.72 s, relaxation delay of 1.0 s, spectral width of 20 ppm and 64 k data points. ^{13}C NMR spectra were recorded with 30° pulses, acquisition time of 0.90 s, relaxation delay of 2.0 s, spectral width of 240 ppm and 64 k data points. All 2D homo- and heteronuclear spectra were recorded with 12 ppm spectral width for ^{1}H, and 170 ppm (multiplicity edited HSQC) or 240 ppm (HMBC) for ^{13}C, and with 2048 (DQF-COSY, ROESY and HBMC) or 1730 (multiplicity edited HSQC) data points in the direct dimension and 512 (DQF-COSY and HMBC) or 256 (ROESY and multiplicity edited HSQC) data points in the indirect dimension. HSQC and HBMC spectra were both acquired with relaxation delay of 1.0 s. All 2D NMR data were zero filled to 1 k and 2 k data points in F1 and F2, respectively, with forward linear prediction employed in F1. Icon NMR (version 4.2, Bruker Biospin, Karlsruhe, Germany) was used for controlling automated NMR data acquisition, and Topspin (version 4.0.6, Bruker Biospin) for NMR data processing.

Table 4
^{1}H NMR (600 MHz) and ^{13}C NMR (150 MHz) spectroscopic data of **13d**, **13f** and **14b** in methanol-d_4 (δ in ppm, J in Hz).

Position	**13d**		**13f**		**14b**	
	δ_C, type[a]	δ_H, mult (J)[b]	δ_C, type[a]	δ_H, mult (J)[b]	δ_C, type[a]	δ_H, mult (J)[b]
1	30.2, CH	1.62, m[c]	30.2, CH	1.62, m[c]	30.2, CH	1.62, m[c]
2	26.8, CH_2	α: 1.56, m[c] β: 1.28, m[c]	26.8, CH_2	α: 1.58, m[c] β: 1.28, m[c]	26.8, CH_2	α: 1.56, m[c] β: 1.26, m[c]
3	20.7, CH_2	1.45, m	20.7, CH_2	1.45, m	20.7, CH_2	1.46, m
4	35.1, CH	2.06, m[c]	35.1, CH	2.06, m[c]	35.1, CH	2.06, m[c]
5	38.2, CH	3.12, d (9.6)	38.0, CH	3.12, d (9.0)	38.2, CH	3.12, d (9.0)
6	132.5, C	–	132.1, C	–	132.5, C	–
7	140.1, CH	7.16, br d (6.3)	140.3, CH	7.17, br s	140.0, CH	7.15, br s
8	26.5, CH_2	α: 2.05, m[c] β: 2.39, m	26.5, CH_2	α: 2.04, m[c] β: 2.39, m	26.5, CH_2	α: 2.04, m[c] β: 2.39, m
9	30.1, CH	1.58, m[c]	30.1, CH	1.58, m[c]	30.1, CH	1.58, m[c]
10	31.6, CH	2.71, q (9.4)	31.7, CH	2.71, q (9.4)	31.6, CH	2.70, q (9.4)
11	48.6, C	–	48.6, C	–	48.6, C	–
12	28.0, CH_2	1.24, m[c]	28.0, CH_2	A: 1.24, m[c] B: 1.29, m[c]	28.2, CH_2	1.28, m[c]
13	22.8, CH_2	A: 1.00, m[c] B: 1.24, m[c]	22.4, CH_2	A: 1.09, m[c] B: 1.22, m[c]	22.7, CH_2	A: 1.04, m B: 1.28, m[c]
14	35.2, CH_2	A: 1.04, m B: 1.26, m[c]	35.2, CH_2	A: 1.13, m[c] B: 1.34, m[c]	35.3, CH_2	A: 1.13, m B: 1.33, m[c]
15	33.6, CH	1.70, m	33.5, CH	1.80, m	33.7, CH	1.80, m
16	69.9, CH_2	3.91, m	70.0, CH_2	A: 3.95, dd (10.7, 6.0) B: 4.00, dd (10.7, 6.7)	70.1, CH_2	4.01, m
17	17.1, CH_3	0.88, d (6.6)	16.9, CH_3	0.93, d (6.6)	17.2, CH_3	0.95, d (6.6)
18	70.2, CH_2	A: 3.65, d (10.7) B: 3.70, d (10.7)	70.1, CH_2	A: 3.66, d (10.7) B: 3.72, d (10.7)	70.2, CH_2	A: 3.66, d (10.7) B: 3.72, d (10.7)
19	172.3, C	–	171.9, C	–	172.2, C	–
20	20.2, CH_3	0.97, d (6.6)	20.2, CH_3	0.95, d (6.6)	20.2, CH_3	0.95, d (6.6)
1′	168.5, C	–	169.0, C	–	168.5, C	–
2′	116.7, CH	5.76, d (12.8)	115.2, CH	6.32, d (15.9)	118.6, CH	6.52, d (15.9)
3′	144.4, CH	6.86, d (12.8)	146.3, CH	7.60, d (15.9)	145.9, CH	7.67, d (15.9)
4′	127.6, C	–	127.4, C	–	135.4, C	–
5′	133.1, CH	7.57, d (8.6)	111.4, CH	7.20, br s	128.9, CH	7.61, br s
6′	115.6, CH	6.75, d (8.6)	150.3, C	–	131.2, CH	7.40, br s
7′	159.7, C	–	149.1, C	–	129.7, CH	7.41, br s
8′	115.6, CH	6.75, d (8.6)	116.2, CH	6.81, d (8.6)	131.2, CH	7.40, br s

(*continued on next page*)

Table 4 (*continued*)

Position	**13d**		**13f**		**14b**	
	δ_C, type[a]	δ_H, mult (J)[b]	δ_C, type[a]	δ_H, mult (J)[b]	δ_C, type[a]	δ_H, mult (J)[b]
9′	133.1, CH	7.57, d (8.6)	123.8, CH	7.07, br dd (8.6, 1.2)	128.9, CH	7.61, br s
10′			56.2, CH_3	3.90, s		

[a] ^{13}C NMR data assigned by HSQC and HMBC experiments.
[b] Multiplicities reported as apparent splittings: s = singlet, d = doublet, q = quartet, m = multiplet, br = broad.
[c] Multiplicities undetermined due to overlapping signals.

2.13. Calculation and acquisition of ECD spectra

The model structure of **11b** was subjected to MacroModel interfaced to Schrödinger Maestro 11.9 (Schrödinger, LLC, USA) for conformational search with the Molecular Merck force field static (MMFFs) in gas phase [27]. Geometry optimization for conformers showing relative energy within 5.02 kcal/mol were performed using the density functional theory (DFT) method with the B3LYP functional and the 6-31G(d, p) basis set of ground state [28,29]. Polarizable continuum model in the integral equation formalism (IEF-PCM) was included for assessment of the acetonitrile solvent effect [30]. The DFT and TDDFT calculations were conducted for lowest-energy conformers accounting for more than 1% Boltzmann distribution with the Gaussian 16 program package [31]. Oscillator strengths and rotatory strengths of the first 60 excited states were calculated at TDDFT CAM-B3LYP/6-31G (d,p) level for each conformer, using IEF-PCM for acetonitrile solvent effect [32]. The overall calculated ECD spectra were created after Boltzmann averaging the calculated spectra of each conformer, which was exported using SpecDis software ver. 1.71 (Berlin, Germany) [33] with a half-bandwidth of 0.30 eV. The calculated ECD spectrum was redshifted by 9 nm. To evaluate the accuracy of absolute configuration assignment, we employed SpecDis to calculate the enantiomeric similarity index (Δ_{ESI}) [34], which facilitated a quantitative comparison of the calculated and experimental ECD spectra.

Experimental ECD spectra of all identified decipiene diterpenoids and ester derivatives were recorded in acetonitrile using a quartz cuvette with 1 cm path length. All measurements were conducted at 25 °C under constant nitrogen gas flow according to the following parameters: wavelength 190–400 nm, scan speed 50 nm/min, digital integration time 4 s, bandwidth 5.0 mm, and 3 accumulations.

2.14. Enzyme kinetics of PTP1B inhibition

To determine the inhibition mode of active ester derivatives of the decipiene diterpenoids, i.e., **13a**, **13b**, **13f** and **14b** against the PTP1B enzyme, various concentrations of each compound were evaluated for their PTP1B inhibition at three different concentrations of *p*-NPP (0.5, 1, and 2 mM), respectively. The kinetic data were analyzed by GraphPad Prism version 9.5.0 (GraphPad Software, Inc.) to be graphically interpreted as Lineweaver-Burk plot, from which the mode of inhibition was determined. Kinetic parameters were calculated by fitting the data to the Michaelis-Menten equation using non-linear regression analysis (GraphPad Prism version 9.5.0, GraphPad Software, Inc.).

2.15. Molecular docking simulation

Molecular docking was performed using Maestro version 13.0 software (Schrödinger, LLC). The 2D structures of the docked compounds were prepared using the 2D sketcher tool available in Maestro, while the 3D structures were generated using the LigPrep module. The X-ray structure of PTP1B in complex with the catalytic inhibitor 3-({5-[(*N*-acetyl-3-{4-[(carboxycarbonyl)(2-carboxyphenyl)amino]-1-naphthyl}-L-alanyl)amino]pentyl}oxy)-2-naphthoic acid (compound C, PDB ID: 1NNY [35]) at a resolution of 2.40 Å was used as reference to investigate the ligand–protein interaction at the catalytic binding site. The co-crystallized structure of PTP1B with an allosteric inhibitor 3-(3,5-dibromo-4-hydroxy-benzoyl)-2-ethyl-benzofuran-6-sulfonic acid (4-sulfamoyl-phenyl)-amide (Compound A, PDB ID: 1T49 [36]) at a resolution of 1.90 Å was used as reference to explore the ligand–protein interaction at the allosteric binding site. Protein receptors were prepared using the Protein Preparation module with default settings and all water molecules removed. The docking grid was created in the Receptor Grid Generation module and defined as an enclosed box centered at the co-crystallized ligand's centroid and sized to match the ligand. Ligand docking and scoring were performed using Glide with default settings and with the SP (standard precision) scoring function. The figures were generated using PyMOL (2.5.2) and Discovery Studio Visualizer v21.1.0.20298.

3. Results and discussion

3.1. Antidiabetic activity screening for acetonitrile extract of E. clarkei

As a part of our continued endeavor to investigate chemical constituents in and pharmacological properties of *Eremophila* spp., the crude acetonitrile extract of *E. clarkei* leaves was assessed for inhibitory activity against PTP1B, α-glucosidase, and α-amylase at a concentration of 50 μg/mL. The crude extract showed strong inhibitory activity against PTP1B with 82.2 ± 2.8 % inhibition, but no inhibitory activity against α-glucosidase and α-amylase with 3.2 ± 0.8 % and 1.0 ± 0.4 % inhibition, respectively. The dose-dependent inhibitory effect of the extract was therefore assessed for PTP1B, which resulted in an IC_{50} value of 33.0 ± 0.8 μg/mL (Table 1 and Fig. S1).

3.2. High-resolution PTP1B inhibition profiling for acetonitrile extract of E. clarkei

A 46-min analytical-scale HPLC method provided satisfactory separation of all major constituents in the crude extract (Fig. 1), and the eluate from 5 to 35 min was microfractionated at a resolution of 2.93 data points per min. Following evaporation, the dried content in each well was tested for PTP1B inhibitory activity, which provided a high-resolution PTP1B inhibition profile (Fig. 1). The biochromatogram shows that the material eluted with peak *12* is correlated with strong PTP1B inhibition (98.3%), the material eluted with peaks *13a–13f* (indicated as fraction *13*) and peaks *14b* and *14c* (indicated as fraction *14*) are correlated with moderate to strong PTP1B inhibition (75% – 95%), and the material eluted with peak *11* is correlated with weak PTP1B inhibition (49.2%).

3.3. Isolation and structure elucidation of compounds from E. clarkei

Automated UV threshold-based collection from analytical scale HPLC separation led to isolation of 23 compounds as detailed in Section 2.10, among which the structures of 20 compounds were elucidated. Comparison of HRMS and NMR data with those reported in literature revealed one known decipiene diterpenoid, 1,18-dihydroxydecipi-14-en-19-oic acid (**11b**) [37], as well as the ten *O*-methylated flavonoids, hispidulin (**2b**) [38], 6-methoxykaempferol 3-methyl ether (**3**) [39], jaceosidin (**4**) [3], 5,7,4′-trihydroxy-3,6,3′,5′-tetramethoxyflavone (**5**) [40], jaceidin (**6**) [41], 3′,5,7-trihydroxy-3,4′,5′-trimethoxyflavone (**7**) [42], 3′,5,7-trihydroxy-3,4′,5′,6-tetramethoxyflavone (**8**) [43], 5,7-dihydroxy-3,3′,4′,6-tetramethoxyflavone (**9**) [43], 5,7-dihydroxy-3,3′,4′,5′-tetramethoxyflavone (**11a**) [44], and 5,7-dihydroxy-3,3′,4′,5′,6-pentamethoxyflavone (**12**) [43] (Table S1). Apart from these compounds, extensive analysis of HRMS as well as 1D and 2D hetero- and homonuclear NMR experiments led to identification of eight previously

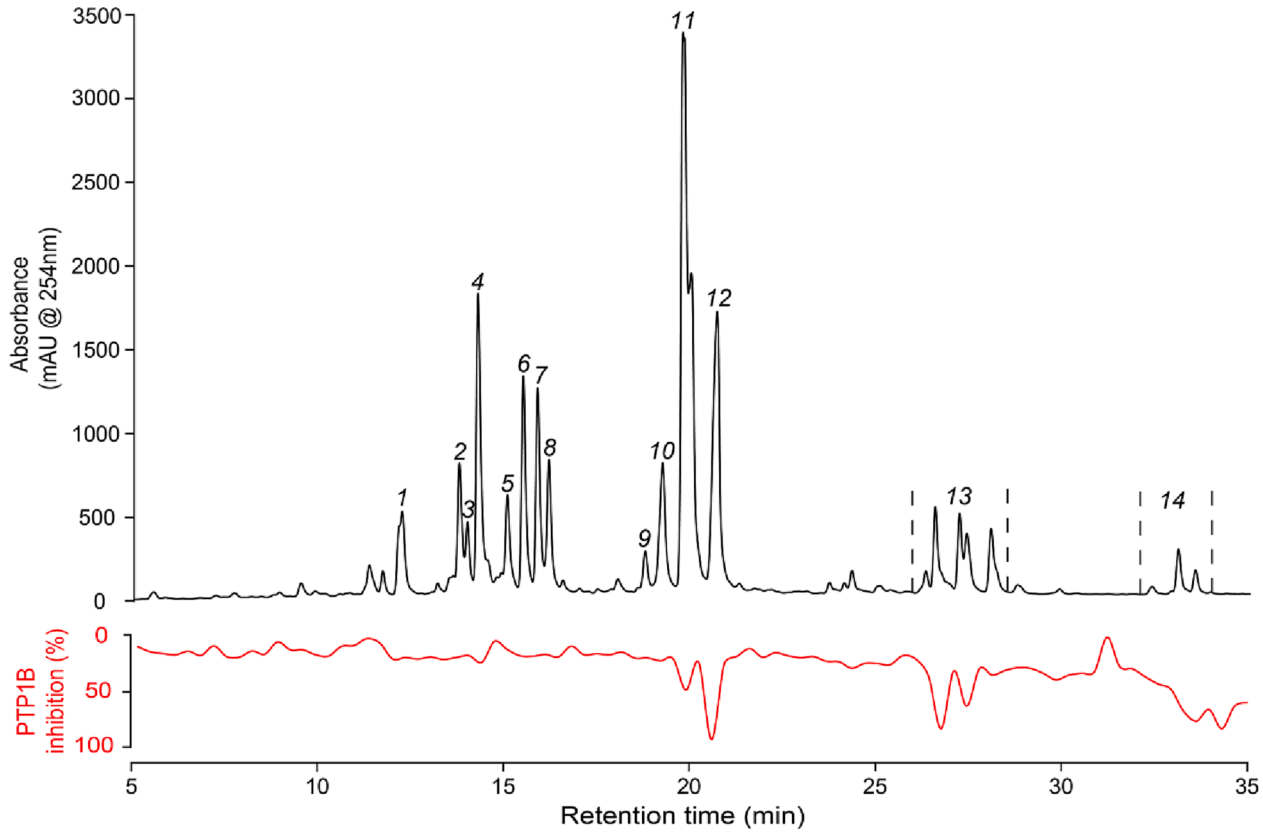

Fig. 1. HPLC chromatogram at 254 nm (top, black) and high-resolution PTP1B inhibition profile (bottom, red) of the acetonitrile extract of *E. clarkei*.

undescribed decipiene diterpenoids, eremoclarkanes A-H, and a biogenetically related phenolic acid, eremoclarkic acid (Fig. 2).

The material eluted with peak *1* showed a $[M-H]^-$ ion with *m/z* 351.2168 (calcd for $C_{20}H_{31}O_5^-$ 351.2177, ΔM +2.6 ppm) (Fig. S7), suggesting the molecular formula $C_{20}H_{32}O_5$, which represents five indices of hydrogen deficiency. The COSY spectrum (Fig. S19) revealed the H_3-20 ↔ H-1 ↔ H_2-2 ↔ H_2-3 ↔ H-4 ↔ H-10 ↔ (H-5)H-9 ↔ (H-1)H-8 ↔ H-7 coupling network shown in Fig. 3, and together with HMBC correlations from H_3-20 to C-9, from H-5 and H-7 to C-6 and C-19 (δ_C 171.8), and from H-4, H-5, H-10, and H_2-18 to C-11 (Fig. 3), this confirmed the presence of the core tricyclo[5.3.1.$0^{5,11}$]undecane ring system substituted with a methyl group at C-1 and a carboxylic acid at C-6. The COSY spectrum additionally revealed the H_2-12 ↔ H_2-13 ↔ H_2-14 ↔ H-15 ↔ (H_2-16)H_3-17 spin system for the side chain of **1**. These two subunits were assembled to be a decipiene skeleton on the basis of HMBC correlation from H-4, H-5, and H_2-18 to C-12 and from H_2-12 to C-4, C-5, and C-11 (Fig. 3). The NMR data of **1** (Table 2) resembled those of the known compound 1,18-dihydroxydecipi-14-en-19-oic acid (**11b**) (Table S1), the main difference being the absence of signals for the H_2-8 methylene signals observed for **11b** and the appearance of a deshielded methine proton H-8 at δ_H 4.22 (1H, br dd, $J = 7.2$, 1.2 Hz, δ_C 67.4) in **1**, suggesting a hydroxyl group at C-8. The ROESY spectrum (Fig. S20) revealed a correlation network between α-oriented H-1 ↔ H-4 ↔ H-9 ↔ H-10(↔H-1) ↔ H-5 ↔ H_2-18 (Fig. 3), and between β-oriented H-8 and H_3-20. Thus, the relative configuration of the core part, i.e., the tricyclo [5.3.1.$0^{5,11}$] undecane ring of **1** is 1*R**,4*S**,5*R**,8*S**,9*R**,10*R**,11*R**.

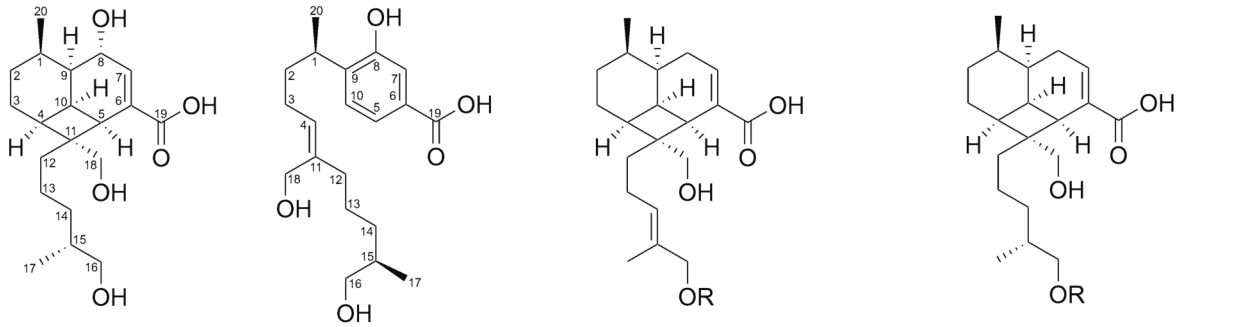

Fig. 2. Structures of previously undescribed decipiene diterpenoids, eremoclarkanes A-H, and eremoclarkic acid identified in acetonitrile extract of *E. clarkei*.

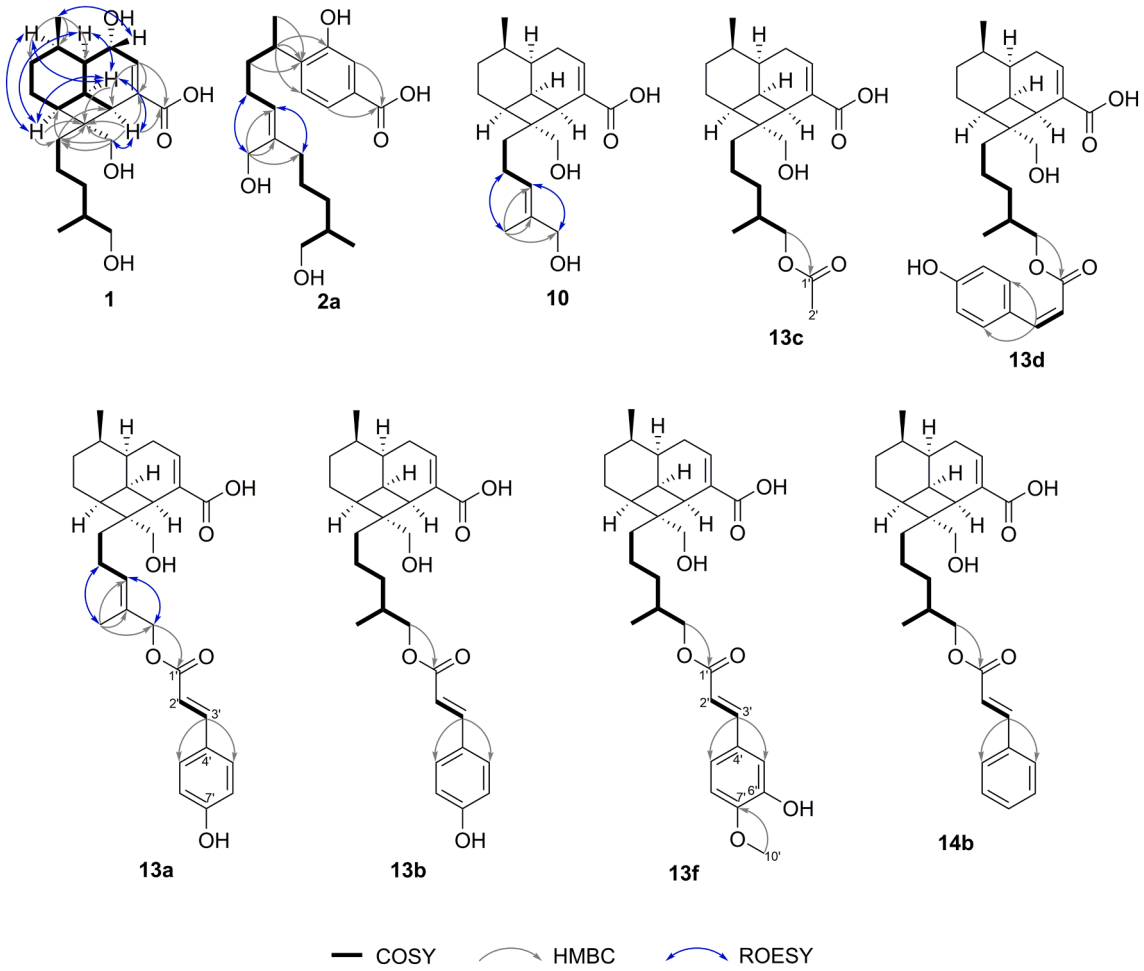

Fig. 3. Selected COSY, HMBC, and ROESY correlations used for structure elucidation of previously undescribed decipiene diterpenoids, eremoclarkanes A-H, and eremoclarkic acid.

The absolute configuration of the tricyclo [5.3.1.$0^{5,11}$] undecane ring moiety in **11b** was determined by comparison of the experimental ECD spectrum of **11b** and the calculated ECD spectrum for the model structure of **11b** (Fig. 4), generated by truncation of the flexible side chain from C-13 to C-17. In the first step, conformational searches were conducted for two possible isomers (1*R**,4*S**,5*R**,9*R**, 10*R**,11*R**)-**11b** model and (1*S**,4*R**,5*S**,9*S**,10*S**,11*S**)-**11b** model, resulting in 24 and 23 conformers, respectively (Tables S2 and S4). After geometry optimization, six dominant conformers (>1% Boltzmann distribution) were obtained for both isomers (Tables S3 and S5), which were submitted to ECD calculations. The experimental ECD spectrum of **11b**, characterized by a strong negative Cotton effect at around 230 nm, perfectly matched the calculated data for the (1*R**,4*S**,5*R**,9*R**,10*R**,11*R**)-**11b** model, with a high enantiomeric similarity index (Δ_{ESI}) of 0.9771. Therefore, the absolute configuration of the tricyclo [5.3.1.$0^{5,11}$] undecane ring moiety in **11b** was determined to be (1*R*,4*S*,5*R*,9*R*,10*R*,11*R*). The experimental ECD spectra of **1** and **11b** were highly similar (Fig. 5), and the core structure of **1** is therefore assigned the 1*R*,4*S*,5*R*,8*S*,9*R*,10*R*,11*R*-configuration. The flexibility of the side chain at C-11 prohibited establishment of the configuration of C-15 in **1** by analysis of ROESY correlations. However, decipiene diterpenoids like **1** and **11b** presumably derive from the same biosynthetic precursor, suggesting conserved configurations of C-1, C-4, C-5, C-8, C-9, C-10, C-11, and C-15. Croft and co-workers previously established the 15*R*-configuration of **11b** by X-ray crystallography [37], and **1** was tentatively assigned the 15*R*-configuration based on biosynthetic arguments. Thus, the structure of **1** was elucidated as (1*R*,4*S*,5*R*,8*S*,9*R*,10*R*,11*R*,15*R*)-8,16,18-trihydroxydecipi-7-en-19-oic acid, for which the name eremoclarkane A is proposed. Fully assigned ^{1}H and ^{13}C NMR data are provided in Table 2, with ^{1}H NMR, HSQC, HMBC, COSY and ROESY spectra presented in Figs. S16-S20.

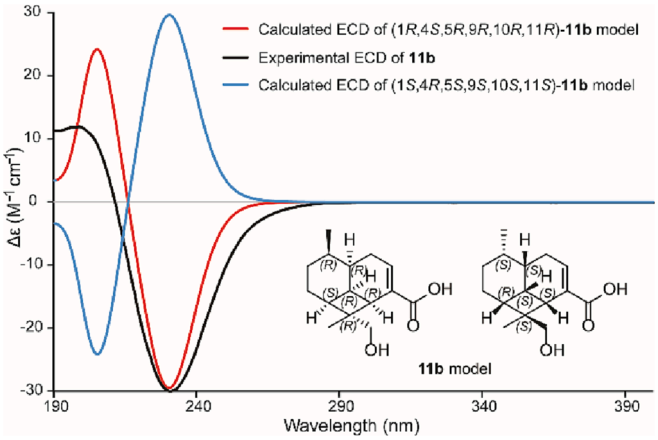

Fig. 4. Comparison of the experimental ECD spectrum of **11b** and the calculated spectrum of the **11b** model compound without the long side chain.

The material eluted with peak *2a* showed a $[M-H]^-$ ion with *m/z* 349.2018 (calcd for $C_{20}H_{29}O_5^-$ 349.2020, ΔM +0.7 ppm) in the HRESIMS spectrum (Fig. S8), suggesting the molecular formula $C_{20}H_{30}O_5$, which represents six indices of hydrogen deficiency. The ^{1}H and 2D homo- and

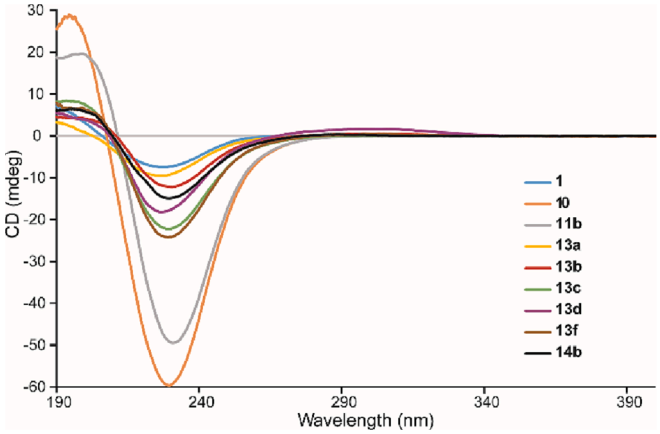

Fig. 5. Experimental ECD spectra of identified decipiene diterpenoids and ester derivatives in acetonitrile.

heteronuclear NMR data analysis of **2a** indicated the presence of a 1,2,4 trisubstituted aromatic ring and a linear terpenoid side chain. The substituted aromatic ring showed an AMX spin system characterized by three aromatic protons resonating at δ_H 7.45 (1H, br d, J = 7.8 Hz, H-5), δ_H 7.41 (1H, br s, H-7) and δ_H 7.18 (1H, br d, J = 7.8 Hz, H-10). The COSY spectrum revealed correlations for the H_3-20 ↔ H-1 ↔ H_2-2 ↔ H_2-3 ↔ H-4 and H_2-12 ↔ H_2-13 ↔ H_2-14 ↔ H-15 ↔ (H_2-16/H_3-17) spin systems of the linear terpenoid side chain. These two moieties were assembled to the entire side chain as shown in Fig. 3 by HMBC correlations from H_2-18 to C-4, C-11, and C-12. The $\Delta^{4,11}$ double bond was shown to have *E*-configuration based on ROESY correlations between H-4 and H_2-12 and between H_2-3 and H_2-18. Finally, the side chain was linked to the trisubstituted aromatic ring on the basis of HMBC correlations from H-1 to C-8, C-9 and C-10 and from H_2-2 and H_3-20 to C-9 (Fig. 3). The structure of **2a** is, *vide infra* (Section 3.4), proposed to derive from the structure of **1**, and C-1 and C-15 in **2a** are therefore tentatively assigned the 1*R*,15*R*-configuration. Thus, the structure of **2a** was elucidated as shown in Fig. 2, for which the name eremoclarkic acid is proposed. ^{1}H and ^{13}C NMR data are provided in Table 2, with the ^{1}H NMR, HSQC, HMBC, COSY, and ROESY spectra presented in Figs. S21-S25.

The material eluted with peak *10* showed a $[M-H]^-$ ion with *m/z* 333.2067 (calcd for $C_{20}H_{29}O_4^-$ 333.2071, ΔM +1.3 ppm) in the HRESIMS spectrum (Fig. S9), suggesting the molecular formula $C_{20}H_{30}O_4$, which represents six indices of hydrogen deficiency. The 1D and 2D NMR data of **10**, showed high similarity with those of **11b** for the tricyclo [5.3.1.0^{5,11}] undecane ring. However, signals for the H_2-14 methylene, H-15 methine, and H_3-17 methyl doublet observed in the ^{1}H NMR spectrum of **11b** were absent in the ^{1}H NMR spectrum of **10**. Instead, an olefinic proton at δ_H 5.30 (1H, t, J = 7.0 Hz, H-14), a methyl singlet at δ_H 1.60 (3H, s, H_3-17) and a quaternary carbon at δ_C 135.1 (C-15) appeared in the ^{1}H NMR or ^{13}C NMR spectra of **10**. HMBC correlations from H_3-17 to C-14 and C-15 confirmed the $\Delta^{14,15}$ double bond, which was assigned the *E*-configuration based on ROESY correlations between H-14 and H_2-16 and between H_2-13 and H_3-17. The experimental ECD spectra of **10** and **11b** showed high similarity (Fig. 5) with large negative Cotton effects around 235 nm, indicating the same absolute configuration of the core skeleton. Thus, the structure of **10** was elucidated as (1*R*,4*S*,5*R*,9*R*,10*R*,11*R*,14*E*)-16,18-dihydroxydecipi-7,14-dien-19-oic acid, for which the name eremoclarkane B is proposed. Fully assigned ^{1}H and ^{13}C NMR data are provided in Table 2, with ^{1}H NMR, ^{13}C NMR, HSQC, HMBC, COSY, and ROESY spectra presented in Figs. S26-S31.

The material eluted with peak *13c* showed a $[M-H]^-$ ion with *m/z* 377.2316 (calcd for $C_{22}H_{33}O_5^-$ 377.2333, ΔM +4.6 ppm) in the HRESIMS spectrum (Fig. S12), suggesting the molecular formula $C_{22}H_{34}O_5$, which represents six indices of hydrogen deficiency. The ^{1}H NMR spectrum of **13c** shows all the same resonances as the ^{1}H NMR spectrum of **11b**, but with additional signals corresponding to an acetyl group (δ_C 172.9, C-1′ and δ_H 2.02, 3H, s, H-2′; δ_C 20.5, C-2′). HMBC correlations from H_2-16 to C-1′ confirmed acetylation at C-16. The experimental ECD spectra of **13c** and **11b** showed high similarity (Fig. 5), and thus the structure of **13c** was elucidated as (1*R*,4*S*,5*R*,9*R*,10*R*,11*R*,15*R*)-16-*O*-acetyl-18-hydroxydecipi-7-en-19-oic acid, for which the name eremoclarkane E is proposed. Fully assigned ^{1}H and ^{13}C NMR data are provided in Table 3, with ^{1}H NMR, HSQC, HMBC, COSY, and ROESY spectra presented in Figs. S43-S47.

The material eluted with peak *13a* showed a $[M-H]^-$ ion with *m/z* 479.2418 (calcd for $C_{29}H_{35}O_6^-$ 479.2439, ΔM +4.4 ppm) in the HRESIMS spectrum (Fig. S10), suggesting the molecular formula $C_{29}H_{36}O_6$, which represents 12 indices of hydrogen deficiency. The ^{1}H NMR spectra of **13a** and **10** showed high similarity in the up-field region (δ_H < 4.00 ppm), indicating that **13a** shares the same decipiene skeleton as **10** – and ROESY correlations between H-14 and H_2-16 and between H_2-13 and H_3-17 confirmed the *E*-configuration of the $\Delta^{14,15}$ double bond for **13a** as well. However, the down-field region (δ_H > 5.00 ppm) of the ^{1}H NMR spectrum of **13a** showed two additional aromatic resonances at δ_H 6.81 (2H, AA'-system) and δ_H 7.46 (2H, XX'-system) as well as two olefinic resonances at δ_H 6.32 (1H, d, J = 15.9 Hz) and δ_H 7.60 (1H, d, J = 15.9 Hz), characteristic of a *trans-p*-coumaroyl unit. HMBC correlations from H_2-16 (δ_H 4.53, 2H, s) to C-1′ (δ_C 169.0) established esterification with the coumaroyl unit at C-16. The experimental ECD spectra of **11b** and **13a** (Fig. 5) show high similarity, and thus the structure of **13a** was elucidated as (1*R*,4*S*,5*R*,9*R*,10*R*,11*R*,14*E*)-16-*O*-*trans-p*-coumaroyl-18-hydroxydecipi-7,14-dien-19-oic acid, for which the name eremoclarkane C is proposed. Fully assigned ^{1}H and ^{13}C NMR data are provided in Table 3, with ^{1}H NMR, HSQC, HMBC, COSY, and ROESY spectra presented in Figs. S32-S36.

The material eluted with peak *13b* and *13d* showed $[M-H]^-$ ions with *m/z* 481.2579 (calcd for $C_{29}H_{37}O_6^-$ 481.2596, ΔM +3.5 ppm) and *m/z* 481.2586 (calcd for $C_{29}H_{37}O_6^-$ 481.2596, ΔM +2.0 ppm), respectively, in the HRESIMS spectrum (Figs. S11 and S13), suggesting the molecular formula $C_{29}H_{38}O_6$ and 11 indices of hydrogen deficiency for both. The ^{1}H NMR spectra of **13b** and **13d** revealed the same characteristic signals as observed for **11b**, confirming both compounds to have the same basic skeleton as **11b**. Both compounds also showed signals for a coumaroyl unit attached to C-16 based on HMBC correlations from H-16 to C-1′ (Fig. 3). However, whereas **13b** showed two olefinic signals confirming the *trans-p*-coumaroyl unit (δ_H 6.31, 1H, d, J = 15.9 Hz, H-2′ and δ_H 7.60, 1H, d, J = 15.9 Hz, H-3′), **13d** showed olefinic signals confirming the *cis-p*-coumaroyl unit (δ_H 5.76, 1H, d, J = 12.8 Hz, H-2′ and δ_H 6.86, 1H, d, J = 12.8 Hz, H-3′). The experimental ECD spectra of **13b** and **13d** show high similarity to that of **11b** (Fig. 5), and thus the structures of **13b** and **13d** were elucidated as (1*R*,4*S*,5*R*,9*R*,10*R*,11*R*,15*R*)-16-*O*-*trans-p*-coumaroyl-18-hydroxydecipi-7-en-19-oic acid and (1*R*,4*S*,5*R*,9*R*,10*R*,11*R*,15*R*)-16-*O*-*cis-p*-coumaroyl-18-hydroxydecipi-7-en-19-oic acid, respectively, for which the names eremoclarkane D (**13b**) and eremoclarkane F (**13d**) are proposed. Fully assigned ^{1}H and ^{13}C NMR data of **13b** and **13d** are provided in Table 3 and Table 4, respectively, with ^{1}H NMR, ^{13}C NMR, HSQC, HMBC, COSY, and ROESY spectra presented in Figs. S37-S42 and Figs. S48-S52.

The material eluted with peak *13f* showed a $[M-H]^-$ ion with *m/z* 511.2680 (calcd for $C_{30}H_{39}O_7^-$ 511.2701, ΔM +4.2 ppm) in the HRESIMS spectrum (Fig. S14), suggesting the molecular formula $C_{30}H_{40}O_7$, which represents 11 indices of hydrogen deficiency. This indicates an additional methoxy group in **13f** compared to **13b**, which was confirmed by the signal for H-10′ at δ_H 3.90 (3H, s). The *trans*-isoferuloyl group was identified based on the characteristic pattern for a 1,2,4-trisubstituted benzene (δ_H 7.20, 1H, br s, H-5′, δ_H 7.07, 1H, br dd, J = 8.6, 1.2 Hz, H-9′, and δ_H 6.81, 1H, d, J = 8.6 Hz, H-8′) together with the *trans*-coupled olefinic signals for H-2′ at δ_H 6.32 (1H, d, J = 15.9 Hz) and H-3′ at δ_H 7.60 (1H, d, J = 15.9 Hz). Selected HMBC and ROESY correlations

used for full structure elucidation are presented in Fig. 3. The experimental ECD spectra of **11b** and **13f** are highly similar, with negative Cotton effects around 235 nm, and thus **13f** was elucidated as (1*R*,4*S*,5*R*,9*R*,10*R*,11*R*,15*R*)-16-*O*-*trans*-*p*-isoferuloyl-18-hydroxydecipi-7-en-19-oic acid, for which the name eremoclarkane G is proposed. Fully assigned ^{1}H and ^{13}C NMR data are provided in Table 4, with ^{1}H NMR, HSQC, HMBC, COSY, and ROESY spectra presented in Figs. S53-S57.

The material eluted with peak *14b* showed a $[M-H]^-$ ion with *m/z* 465.2626 (calcd for $C_{29}H_{37}O_5^-$ 465.2646, ΔM +4.4 ppm) in the HRESIMS spectrum (Fig. S15), suggesting the molecular formula $C_{29}H_{38}O_5$, which represents 11 indices of hydrogen deficiency. Full analysis of 2D homo- and heteronuclear experiments identified **14b** as an esterification product of **11b**, similar to **13b**, **13c**, **13d**, and **13f**. The *trans*-*p*-cinnamoyl unit in **14b** was confirmed by the two olefinic resonances for H-2′ at δ_H 6.52 (1H, d, $J = 15.9$ Hz) and H-3′ at δ_H 7.67 (1H, d, $J = 15.9$ Hz) as well as the resonances observed for H-5′-H-9′. The experimental ECD spectrum of **14b** had the same overall pattern as that of **11b**, and thus the structure of **14b** was elucidated as (1*R*,4*S*,5*R*,9*R*,10*R*,11*R*,15*R*)-16-*O*-*trans*-*p*-cinnamoyl-18-hydroxydecipi-7-en-19-oic acid, for which the name eremoclarkane H is proposed. Assigned ^{1}H and ^{13}C NMR data are provided in Table 4, with ^{1}H NMR, HSQC, HMBC, COSY, and ROESY spectra presented in Figs. S58-S62.

The material eluted with peaks *13e*, *14a* and *14c* showed $[M-H]^-$ ions with *m/z* 511.2677 (calcd for $C_{30}H_{39}O_7^-$ 511.2701, ΔM +4.8 ppm), 463.2472 (calcd for $C_{29}H_{35}O_5^-$ 463.2490, ΔM +3.9 ppm), and 465.2627 (calcd for $C_{29}H_{37}O_5^-$ 465.2646, ΔM +4.2 ppm), respectively, which suggested a molecular formula of $C_{30}H_{40}O_7$ for **13e**, $C_{29}H_{36}O_5$ for **14a** and $C_{29}H_{38}O_5$ for **14c**. This indicates these three compounds to be decipiene diterpenoids as well. However, structural elucidation of these failed due to the low signal-to-noise ratio of their NMR spectra.

3.4. Plausible enzymatic as well as photochemically driven steps involved in decipiene metabolism

Although more than 200 structurally diverse diterpenoids have been identified from different *Eremophila* species [2], investigation of their biosynthesis is scarce. The single previous biosynthetic study available reported (*Z*,*Z*,*Z*)-nerylneryl pyrophosphate (NNPP) as the non-canonical terpene precursor of serrulatane, viscidane, and cembrane diterpenoids in *E. lucida*, *E. drummondii* and *E. denticulata* [45]. Structural analyses of acyclic diterpenes present in *E. glutinosa* and *E. exilifolia* also supported their biosynthesis from NNPP [46,47]. As first proposed by Ghisalberti, the biosynthesis of decipiene diterpenes may involve a cationic intermediate equivalent to the bisabolyl cation crucial in the construction of an array of diverse and complex architectures found in sesquiterpenoids [46,48]. In contrast to the above-mentioned classes of diterpenoids, which are all made with (*Z*,*Z*,*Z*)-NNPP as precursor, the bisabolyl-type sesquiterpenoid cation is built with (*E*,*E*)-farnesyldiphosphate [48]. In biosynthesis of the decipiene diterpenoids, the equivalent C_{20} precursor

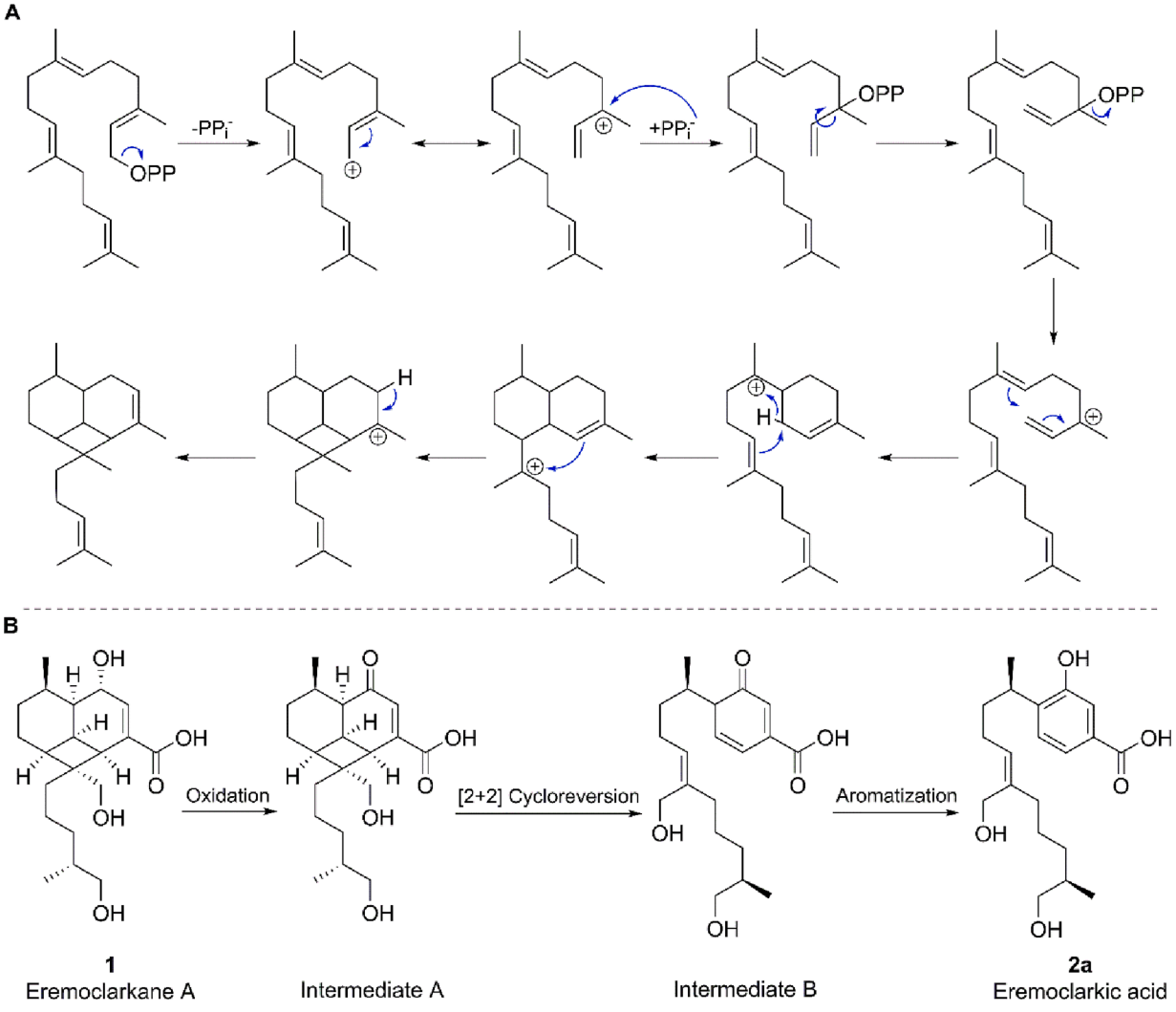

Scheme 1. **A**. Plausible biosynthetic route for formation of the decipiene core skeleton. **B**. Plausible metabolic conversion of **1** into **2a**.

would therefore be (*E,E,E*)-geranylgeranyl pyrophosphate (GGPP). The bisabolyl-type diterpenoid cation formed would give rise to a bicyclic intermediate and a [2+2] Diels-Alder type reaction would generate the decipiene core structure (Scheme 1A). None of the biosynthetic enzymes involved in core structure formation, including diterpene synthases and possibly a [2+2] Diels-Alderase, have been identified so far. Likewise, cytochrome P450s, flavine monooxygenases or α-ketoglutarate dependent dioxygenases involved in oxygenation of the decipiene core structure as well as the acyl-transferases further expanding the decoration pattern all remain unidentified. However, in this context, it should be noted, that many cyclobutane rings in natural products are thought to arise from photochemical reactions [49,50]. Insights from quantum chemistry calculations may serve to more precisely characterize the specific nature of the cyclization reaction giving rise to the tricyclic decipiene core structure [49].

In 1981, Croft et al. demonstrated experimentally, that a decipiene diterpenoid isolated from *E. decipiens* could be converted into a bicyclic compound by UV irradiation [46,51]. In a similar photochemical process, eremoclarkic acid (**2a**) isolated from *E. clarkei* in this study, may be considered derived from **1** in a retro [2+2] Diels-Alder type reaction accompanied by enolization and aromatization (Scheme 1B). Whether these latter reactions proceed non-enzymatically in the oxidative and light-exposed environment of the trichome cells at the surface of the *E. clarkei* leaves or whether the process is catalyzed by a retro [2+2] Diels-Alderase remain to be elucidated.

Enzyme catalyzed Diels-Alder reactions have been shown to be involved in the biosynthesis of several natural products [52,53]. The characterized Diels-Alderases involved were catalyzing 4+2 cycloadditions. However, a cyclase that catalyzes competing [2+2] and [4+2] cycloadditions has recently been characterized [54]. Directed engineering enabled a shift in the catalytic activity of the cyclase towards [2+2] activity. The reverse process, a retro-[2+2] cycloaddition, has also been shown to be enzyme catalyzed [55]. It thus remains to be established whether the formation of the tricyclic decipiene ring system and its further metabolism proceeds as photochemical or enzyme catalyzed reactions.

3.5. Structure-activity relationship of isolated compounds

All metabolites isolated from *E. clarkei* were evaluated for PTP1B inhibitory activity, initially at a concentration of 100 μM, and the percentage inhibition can be seen in Table 5. For compounds displaying more than 50% inhibition at this concentration, i.e., **2b**, **4**, **12**, **13a**, **13b**, **13f** and **14b**, dose-dependent effects were determined, and the results are given as IC_{50} values in Table 5, with corresponding dose-dependent curves provided in Fig. S63.

Among all identified *O*-methylated flavonoids in this study, hispidulin (**2b**) showed the strongest inhibition against PTP1B with an IC_{50} value of 24.8 ± 1.9 μM. Hispidulin has previously been reported as a PTP1B inhibitor with $IC_{50} > 33$ μM [56]. Other *O*-methylated flavonoids showed much weaker PTP1B inhibition than **2b**. Comparison of **3** and **2b** or **6** and **4**, show, that the inhibitory activity decreases significantly when a methoxy group is introduced at C-3. This trend was also observed in some other *O*-methylated flavonoids, including **5**, **7**, **8**, **9**, and **11a**. Interestingly, **12** which harbors a methoxy group at C-3 displayed similar inhibitory activity to **4**, indicating that the introduction of methoxy groups to C-3′, C-4′ and C-5′ might compensate for the decline in activity due to the presence of methoxy group at C-3. Comparison of **4** and **2b** shows, that the inhibitory activity decreases approximately by a factor of two when a methoxy group is added at C-3′. Comparison of **7** and **8** or **11a** and **12** demonstrates that absence of the methoxy group at C-6 might lead to decreased inhibitory activity.

The decipiene diterpenoids **1**, **10**, and **11b** were inactive against PTP1B. However, the ester derivatives of decipiene diterpenoids, i.e., **13a**, **13b**, **13f**, and **14b** showed PTP1B inhibitory activity with IC_{50} values ranging from 22.8 ± 2.3 to 33.6 ± 8.8 μM as seen in Table 5. This indicates that the *trans-p*-coumaroyl unit in **13a** and **13b**, the *trans-p*-isoferuloyl in **13f**, and the *trans-p*-cinnamoyl in **14b** might contribute to the increased inhibitory activity. Surprisingly, the *cis-p*-coumaroyl decipiene diterpenoid **13d** showed five times weaker PTP1B inhibitory activity with 20.3 ± 2.5 % inhibition at 100 μM compared to the *trans-p*-coumaroyl analogue **13b** with 103.9 ± 3.0 % inhibition at the same concentration. This implies that change of configuration of the $\Delta^{2',3'}$ double bond of the *p*-coumaroyl unit from *trans* to *cis* might result in decreased inhibitory activity. This is supported by a previous study which reported weaker PTP1B inhibitory activity of the triterpenoid 3β-*O*-*cis-p*-coumaroyl-2α-hydroxy-urs-12-en-28-oic acid containing a *cis-p*-coumaroyl unit (IC_{50} = 26.67 ± 0.35 μM) than its *trans*-isomer jacoumaric acid (IC_{50} = 11.93 ± 0.31 μM) [21]. In a recent study, we showed that serrulatane ferulate esters reveal a saddle-shape-like binding in the active site of PTP1B, and that a *cis*-ferulate ester side chain forces the compound to adopt a less favourable conformation than a *trans*-ferulate ester side chain [57]. Additionally, **13c** exhibited stronger PTP1B inhibitory activity with 10.3 ± 1.5 % inhibition at 100 μM compared to its non-acetylated analogue **11b** with −1.3 ± 3.1 % inhibition at the same concentration, which supports that acetylation of the decipiene scaffold might positively impact the PTP1B inhibitory activity.

Table 5
Inhibitory activity of identified compounds against PTP1B.

Compound	PTP1B inhibition (% at 100 μM)[a]	IC_{50} (μM) against PTP1B[a]	K_i (μM)	Mode of inhibition
1	10.3 ± 1.3	–	–	–
2a	10.6 ± 6.1	–	–	–
2b	122.9 ± 2.1	24.8 ± 1.9	–	–
3	9.3 ± 3.0	–	–	–
4	67.0 ± 4.4	>100	–	–
5	15.9 ± 5.6	–	–	–
6	18.1 ± 3.6	–	–	–
7	11.1 ± 3.0	–	–	–
8	38.0 ± 9.0	–	–	–
9	17.1 ± 3.3	–	–	–
10	−3.3 ± 1.8	–	–	–
11a	−0.5 ± 1.2	–	–	–
11b	−1.3 ± 3.1	–	–	–
12	66.5 ± 6.4	>100	–	–
13a	102.5 ± 3.7	33.6 ± 8.8	21.3	Competitive
13b	103.9 ± 3.0	25.9 ± 7.3	24.9	Competitive
13c	10.3 ± 1.5	–	–	–
13d	20.3 ± 2.5	–	–	–
13f	100.2 ± 1.1	22.8 ± 2.3	22.3	Mixed
14b	95.8 ± 0.6	29.1 ± 3.6	36.6	Mixed
[b]RK-682	–	14.3 ± 1.2	–	–

[a] Results reported as mean ± standard error of three independent measurements.
[b] Positive control.

3.6. Enzyme kinetics analysis of PTP1B inhibition

The enzyme kinetics analysis of PTP1B inhibition was performed at different concentrations of the *p*-NPP substrate in the absence and presence of various concentrations of investigated inhibitors. The obtained enzyme kinetics data were analyzed by Lineweaver-Burk plot to determine the mode-of-action for PTP1B inhibition [21]. The results reveal that **13a** and **13b** are competitive inhibitors, because all straight lines in Fig. 6A and 6B cross the same *y*-intercept. Thus, as inhibitor concentration increased, K_m increased, and V_{max} remained unchanged, and inhibition constant values (K_i) of 21.3 and 24.9 μM (Table 5) were obtained for **13a** and **13b**, respectively. The straight lines in both Lineweaver-Burk plot of **13f** and **14b** (Fig. 6C and 6D) intersect above *x*- and to the left of *y*-axis, indicating mixed-mode inhibition (as inhibitor concentration increased, K_m increased whereas V_{max} decreased). These two inhibitors showed K_i values of 22.3 and 36.6 μM (Table 5), respectively.

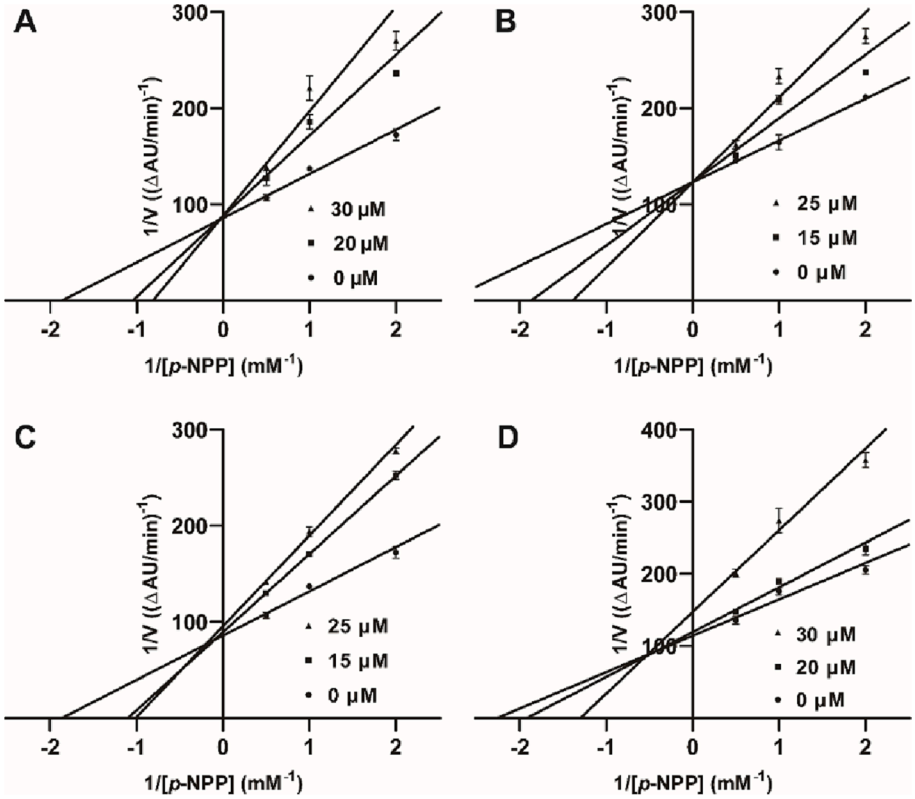

Fig. 6. Lineweaver-Burk plots for PTP1B inhibition by **13a** (**A**), **13b** (**B**), **13f** (**C**) and **14b** (**D**).

3.7. Molecular docking simulation of PTP1B inhibition

The active site of PTP1B is formed by a deep and solvent-accessible pocket that is surrounded by several loops within its catalytic domain, which are crucial for substrate recognition and enzyme activity. These mainly include WPD loop (Thr177-Pro185), P loop (His214-Arg221), Q loop (Gln262), R loop (Val113-Ser118), S loop (Ser201-Gly209) and pTyr loop (Tyr46-Val49) [58–60]. Moreover, the enzymatic activity of PTP1B can be regulated by inducing conformational changes through the binding of ligands to its secondary and allosteric binding sites. The secondary site, also called the second aryl phosphate-binding site, which is composed of key residues Arg24 and Arg254, is an important non-conserved site that regulates the substrate specificity [59,60]. The allosteric binding site includes the α3 helix (Glu186-Glu200), α6 helix (Ala264-Ile281), and α7 helix (Val287-Ser295) [36,59].

The enzyme kinetics studies, *vide ultra*, revealed **13a** and **13b** to be competitive inhibitors, and molecular docking simulations were therefore conducted to investigate the interaction of these two with the catalytic binding site of PTP1B. In general, **13a** and **13b** displayed a significant binding overlap with compound C, a potent and selective PTP1B inhibitor discovered by Szczepankiewicz et al. using linked-fragment strategy [35], in the catalytic site of PTP1B. The binding of compound C with PTP1B extends from the active site to the secondary site, while **13a** and **13b** only occupy the active site (Fig. 7A and 7B). The carboxylate group of the tricyclo[5.3.1.$0^{5,11}$]undecane ring of **13a** formed hydrogen bonds with the backbone of residues S216, A217, G218, I219, and G220, and with the side chain of residue C215 at the active site. Moreover, a hydrogen bond interaction was observed between the carbonyl oxygen of the ester in **13a** and the catalytic residue T263. The terminal phenyl ring in **13a** showed a *T*-shaped π-π interaction with residue F182 in the WPD loop. In addition, the decipiene scaffold of **13a** was involved in hydrophobic interactions with surrounding residues Y46, W179, A217, and I219 (Fig. 7D). Similarly, several hydrogen bond interactions were formed between the carboxylate group of the tricyclo[5.3.1.$0^{5,11}$]undecane ring of **13b** and residues C215, S216, A217, G218, G220, and R221 of the active site. Several hydrophobic interactions were also observed between the tricyclo [5.3.1.$0^{5,11}$]undecane ring in **13b** and the surrounding residues Y46, A217, and I219 (Fig. 7E).

Since **13f** and **14b** were found to be mixed-type inhibitors, *vide ultra*, docking simulations for these two compounds were performed for both the catalytic and the allosteric binding sites. At the catalytic site, **13f** (Fig. 7C and 7F) and **14b** (Fig. 7G and 7J) displayed binding conformations and interactions with PTP1B similar to those seen for **13a**. Interestingly, the phenolic hydroxy group on the terminal phenyl ring of **13f** formed a hydrogen bond with ASP265 (Fig. 7F). This may explain the differences in inhibitory activities among **13c-f**, which share the same core skeleton but have structurally different side chains. Compound **13c** lacks the terminal phenyl ring and corresponding hydrogen bond as seen for **13f**, whereas **13d** possesses a terminal *cis*-4-hydroxycinnamoyl unit. According to the docking pose of **13f**, the *cis*-4-hydroxycinnamoyl unit is likely to cause a steric clash with the binding site, and thereby impairing the binding of **13d** to PTP1B. At the allosteric site, **13f** and **14b** exhibit substantial overlap with compound A, a novel and selective PTP1B allosteric inhibitor reported by Wiesmann et al [36], by forming similar interactions with important residues in the α3 and α6 helixes (Fig. 7H and 7I). The carboxylate group of the tricyclo [5.3.1.$0^{5,11}$]undecane ring of **13f** formed a salt bridge with side chain residue K197 (α3 helix) and a hydrogen bond with residue N193 (α3 helix). The hydroxymethyl group of the tricyclo[5.3.1.$0^{5,11}$]undecane ring of **13f** showed a hydrogen bond interaction with the backbone residues E200 (α3 helix) and K197 (Fig. 7K). As illustrated in Fig. 7L, **14b** binds to the allosteric site of PTP1B in a similar manner as **13f**. The ligand interactions of **14b** at the allosteric site include a salt bridge to the carboxylate group of residue K197, and hydrogen bonds to residues N193 and K197, as well as hydrogen bonds from the hydroxymethyl

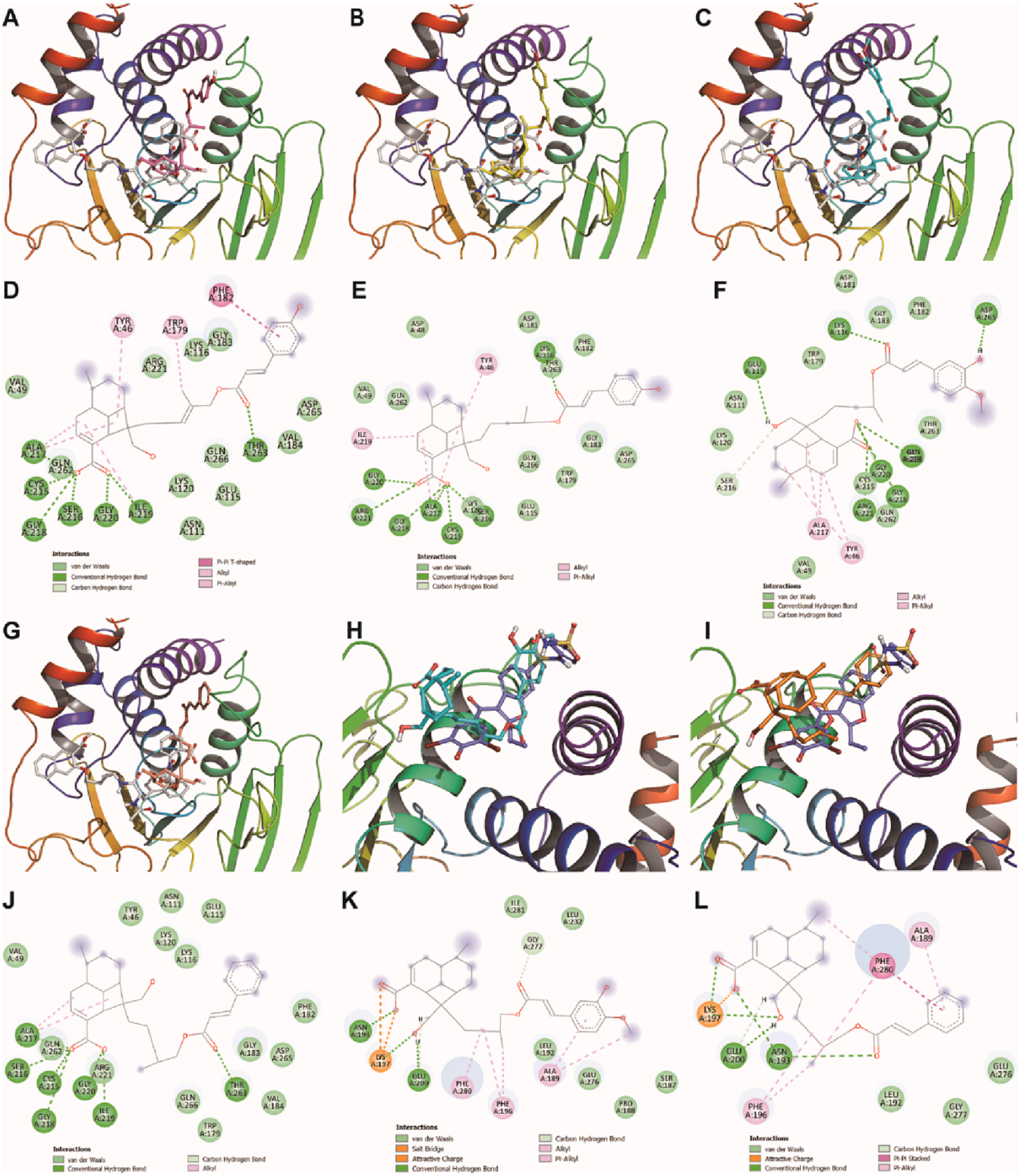

Fig. 7. Molecular docking simulation for PTP1B inhibition of **13a** (magenta stick), **13b** (yellow stick), **13f** (cyan stick), **14b** (orange stick), compound C (white stick) and compound A (purple stick). Superimposition of docked **13a** (**A**), **13b** (**B**), **13f** (**C**), or **14b** (**G**) into the PTP1B catalytic binding site and X-ray structure of compound C bound to the PTP1B catalytic binding site. Superimposition of docked **13f** (**H**), or **14b** (**I**) into the PTP1B allosteric binding site and X-ray structure of compound A bound to the PTP1B allosteric binding site. 2D ligand interaction diagram of **13a** (**D**), **13b** (**E**), **13f** (**F**), and **14b** (**J**) at the catalytic binding site, and **13f** (**K**) and **14b** (**L**) at the allosteric binding site.

group to residues K197 and E200. Moreover, a hydrogen bond interaction was observed between the carbonyl oxygen of the ferulate ester and side chain residue N193. The tricyclo[5.3.1.0^{5,11}]undecane ring, the long alkyl chain, and the terminal phenyl ring of both **13f** and **14b** formed hydrophobic interactions with residues A189 and F196 in the α3 helix and with F280 in the α6 helix (Fig. 7K and 7L). This may also explain the low inhibitory activities of **13c** and **13d** compared to **13f**, as the absence of a hydroxycinnamoyl unit in **13c** and the *cis*-configuration of the 4-hydroxycinnamoyl unit in **13d** may impair these hydrophobic interactions in allosteric sites.

In general, for the strongest PTP1B-inhibiting decipiene esters **13a**, **13b**, **13f**, and **14b**, the core decipiene skeleton was found to form multiple hydrogen bonds and hydrophobic interactions within the catalytic and allosteric binding sites. These interactions are considered fundamental in the protein–ligand interaction, and therefore might account for the inhibitory activity of these compounds. The docking results were in accordance with results from the enzyme kinetics analysis and demonstrated substantial binding capacity of **13a**, **13b**, **13f**, and **14b** to the catalytic and allosteric site of PTP1B enzyme, indicating the ester derivatives of decipiene diterpenoids to be a new class of natural-products-based compounds for development of PTP1B inhibitors.

4. Conclusion

In conclusion, high-resolution PTP1B inhibition profiling combined with repeated analytical-scale HPLC separation led to identification of eight previously undescribed decipiene diterpenoids and ester derivatives thereof as well as a biogenetically related new phenolic acid, from an acetonitrile extract of *E. clarkei*. In addition, one known decipiene diterpenoid and ten known *O*-methylated flavonoids were identified. Among all identified metabolites, the *O*-methylated flavonoid hispidulin (**2b**) and ester derivatives of decipiene diterpenoids harboring a *trans-p*-coumaroyl (**13a** and **13b**), a *trans-p*-isoferuloyl (**13f**) or a *trans-p*-cinnamoyl (**14b**) moiety showed PTP1B inhibitory activity. The enzyme kinetics studies indicated that **13a** and **13b** were competitive PTP1B inhibitors, while **13f** and **14b** showed mixed-type PTP1B inhibition. The molecular docking simulation revealed comparable binding affinity of **13a**, **13b**, **13f**, and **14b** towards the PTP1B enzyme, supporting the results from *in vitro* PTP1B inhibition assay. These are the first decipiene ester derivatives identified and the first study to report this class of compounds as potential PTP1B inhibitors. This expands the diterpenoid chemical space from the genus *Eremophila* and may provide promising leads for development of future therapeutic agents for T2D.

Declaration of Competing Interest

The authors declare the following financial interests/personal relationships which may be considered as potential competing interests: Dan Staerk reports financial support was provided by Novo Nordisk Foundation.

Data availability

Data will be made available on request.

Acknowledgments

The HPLC equipment was obtained via a grant from The Carlsberg Foundation. The HPLC-PDA-HRMS and NMR instruments were acquired through a grant from "Apotekerfonden af 1991", The Carlsberg Foundation, and the Danish Agency for Science, Technology and Innovation via the National Research Infrastructure funds. The Novo Nordisk Foundation is acknowledged for support to the project (grant no. NNF16OC0021616).

Appendix A. Supplementary data

Supplementary data to this article can be found online at https://doi.org/10.1016/j.bioorg.2023.106744.

References

[1] R.J. Chinnock, *Eremophila* and Allied Genera: A Monograph of the Plant Family Myoporaceae, 1st ed., Rosenberg Publishing, Dural, NSW, Australia, 2007.
[2] A.N. Singab, F.S. Youssef, M.L. Ashour, M. Wink, The genus *Eremophila* (Scrophulariaceae): an ethnobotanical, biological and phytochemical review, J. Pharm. Pharmacol. 65 (2013) 1239–1279.
[3] A.A. Algreiby, K.A. Hammer, Z. Durmic, P. Vercoe, G.R. Flematti, Antibacterial compounds from the Australian native plant *Eremophila glabra*, Fitoterapia 126 (2018) 45–52.
[4] E.C. Barnes, A.M. Kavanagh, S. Ramu, M.A. Blaskovich, M.A. Cooper, R.A. Davis, Antibacterial serrulatane diterpenes from the Australian native plant *Eremophila microtheca*, Phytochemistry 93 (2013) 162–169.
[5] I.J. Biva, C.P. Ndi, S.J. Semple, H.J. Griesser, Antibacterial performance of terpenoids from the Australian plant *Eremophila lucida*, Antibiotics 8 (2019) 63.
[6] O.F. Anakok, C.P. Ndi, M.D. Barton, H.J. Griesser, S.J. Semple, Antibacterial spectrum and cytotoxic activities of serrulatane compounds from the Australian medicinal plant *Eremophila neglecta*, J. Appl. Microbiol. 112 (2011) 197–204.
[7] Q. Liu, D. Harrington, J.L. Kohen, S. Vemulpad, J.F. Jamie, Bactericidal and cyclooxygenase inhibitory diterpenes from *Eremophila sturtii*, Phytochemistry 67 (12) (2006) 1256–1261.
[8] Y. Tahtah, S.G. Wubshet, K.T. Kongstad, A.M. Heskes, I. Pateraki, B.L. Møller, A. K. Jäger, D. Staerk, High-resolution PTP1B inhibition profiling combined with high-performance liquid chromatography–high-resolution mass spectrometry–solid-phase extraction–nuclear magnetic resonance spectroscopy: Proof-of-concept and antidiabetic constituents in crude extract of *Eremophila lucida*, Fitoterapia 110 (2016) 52–58.
[9] S.G. Wubshet, Y. Tahtah, A.M. Heskes, K.T. Kongstad, I. Pateraki, B. Hamberger, B. L. Møller, D. Staerk, Identification of PTP1B and α-glucosidase inhibitory serrulatanes from *Eremophila* spp. by combined use of dual high-resolution PTP1B and α-glucosidase inhibition profiling and HPLC-HRMS-SPE-NMR, J. Nat. Prod. 79 (2016) 1063–1072.
[10] C. Liang, C. Ndi, L. Kjaerulff, S. Semple, B. Buirchell, S. Coriani, B.L. Møller, D. Staerk, Characterization of serrulatane diterpenoids in *Eremophila phyllopoda* subsp. *phyllopoda* by triple high-resolution α-glucosidase/PTP1B/radical scavenging profiling, NMR spectroscopy, DFT-GIAO NMR, and electronic circular dichroism calculations, J. Nat. Prod. 86 (2023) 694–709.
[11] A. Brown, B. Buirchell, A Field Guide to the Eremophilas of Western Australia, 1st ed, Simon Nevill Publications, Hamilton Hill, Western Australia, 2011.
[12] P. Coates, E.L. Ghisalberti, P.R. Jefferies, The chemistry of *Eremophila* spp. VIII* a cembrenetriol from *E. clarkei*, Aust. J. Chem. 30 (1977) 2717–2721.
[13] American Diabetes Association, Diagnosis and classification of diabetes mellitus, Diabetes Care 36 (2013) S67–S74.
[14] H.E. Lebovitz, Type 2 diabetes: an overview, Clin. Chem. 45 (1999) 1339–1345.
[15] M. Korc, Update on diabetes mellitus, Dis. Markers 20 (3) (2004) 161–165.
[16] Z.-Y. Zhang, Drugging the undruggable: therapeutic potential of targeting protein tyrosine phosphatases, Acc. Chem. Res. 50 (2017) 122–129.
[17] T.O. Johnson, J. Ermolieff, M.R. Jirousek, Protein tyrosine phosphatase 1B inhibitors for diabetes, Nat. Rev. Drug Discov. 1 (9) (2002) 696–709.
[18] G. Liu, Z. Xin, H. Liang, C. Abad-Zapatero, P.J. Hajduk, D.A. Janowick, B. G. Szczepankiewicz, Z. Pei, C.W. Hutchins, S.J. Ballaron, M.A. Stashko, T. H. Lubben, C.E. Berg, C.M. Rondinone, J.M. Trevillyan, M.R. Jirousek, Selective protein tyrosine phosphatase 1B inhibitors: targeting the second phosphotyrosine binding site with non-carboxylic acid-containing ligands, J. Med. Chem. 46 (2003) 3437–3440.
[19] S. De Munter, M. Köhn, M. Bollen, Challenges and opportunities in the development of protein phosphatase-directed therapeutics, ACS Chem. Biol. 8 (1) (2013) 36–45.
[20] C. Liang, L. Kjaerulff, P.R. Hansen, K.T. Kongstad, D. Staerk, Dual high-resolution α-glucosidase and PTP1B inhibition profiling combined with HPLC-PDA-HRMS-SPE-NMR analysis for the identification of potentially antidiabetic chromene meroterpenoids from *Rhododendron capitatum*, J. Nat. Prod. 84 (2021) 2454–2467.
[21] C. Liang, D. Staerk, K.T. Kongstad, Potential of *Myrtus communis* Linn. as a bifunctional food: Dual high-resolution PTP1B and α-glucosidase inhibition profiling combined with HPLC-HRMS and NMR for identification of antidiabetic triterpenoids and phloroglucinol derivatives, J. Funct. Foods 64 (2020), 103623.
[22] Y. Zhao, K.T. Kongstad, A.K. Jäger, J. Nielsen, D. Staerk, Quadruple high-resolution α-glucosidase/α-amylase/PTP1B/radical radical scavenging profiling combined with high-performance liquid chromatography–high-resolution mass spectrometry–solid-phase extraction–nuclear magnetic resonance spectroscopy for identification of antidiabetic constituents in crude root bark of *Morus alba* L, J. Chromatogr. A 1556 (2018) 55–63.
[23] L. Okutan, K.T. Kongstad, A.K. Jäger, D. Staerk, High-Resolution α-amylase assay combined with high-performance liquid chromatography–solid-phase extraction–nuclear magnetic resonance spectroscopy for expedited identification of α-amylase inhibitors: proof of concept and α-amylase inhibitor in Cinnamon, J. Agric. Food Chem. 62 (2014) 11465–11471.
[24] Y. Tahtah, K.T. Kongstad, S.G. Wubshet, N.T. Nyberg, L.H. Jønsson, A.K. Jäger, Q. Sun, D. Staerk, Triple aldose reductase reductase/α-glucosidase/radical

scavenging high-resolution profiling combined with high-performance liquid chromatography-high-resolution mass spectrometry–solid-phaseextraction–nuclear magnetic resonance spectroscopy for identification of antidiabetic constituents in crude extract of Radix Scutellariae, J. Chromatogr. A 1408 (2015) 125–132.
[25] H.A. Pedersen, C. Ndi, S.J. Semple, B. Buirchell, B.L. Møller, D. Staerk, PTP1B-inhibiting branched-chain fatty acid dimers from *Eremophila oppositifolia* subsp. *angustifolia* identified by high-resolution PTP1B inhibition profiling and HPLC-PDA-HRMS-SPE NMR analysis, J. Nat. Prod. 83 (5) (2020) 1598–1610.
[26] M.N. Beidokhti, E.S. Lobbens, P. Rasoavaivo, D. Staerk, A.K. Jäger, Investigation of medicinal plants from Madagascar against DPP-IV linked to type 2 diabetes, S. Afr. J. Bot. 115 (2018) 113–119.
[27] M. Habgood, T. James, A. Heifetz, Conformational Searching with Quantum Mechanics. In *Quantum Mechanics in Drug Discovery;* Heifetz, A., Eds.; Methods in Molecular Biology; Humana Press Inc., New York, 2020; Vol. *2114*, pp. 207–229.
[28] G. Pescitelli, T. Bruhn, Good computational practice in the assignment of absolute configurations by TDDFT calculations of ECD spectra, Chirality 28 (6) (2016) 466–474.
[29] I. Warnke, F. Furche, Circular dichroism: electronic, Wires Comput. Mol. Sci. 2 (1) (2012) 150–166.
[30] J. Tomasi, B. Mennucci, R. Cammi, Quantum mechanical continuum solvation models, Chem. Rev. 105 (8) (2005) 2999–3094.
[31] M.J. Frisch, G.W. Trucks, H.B. Schlegel, G.E. Scuseria, M.A. Robb, J.R. Cheeseman, G. Scalmani, V. Barone, G.A. Petersson, H. Nakatsuji, X. Li, M. Caricato, A. V. Marenich, J. Bloino, B.G. Janesko, R. Gomperts, B. Mennucci, H.P. Hratchian, J. V. Ortiz, A.F. Izmaylov, J.L. Sonnenberg, D. Williams-Young, F. Ding, F. Lipparini, F. Egidi, J. Goings, B. Peng, A. Petrone, T. Henderson, D. Ranasinghe, V. G. Zakrzewski, J. Gao, N. Rega, G. Zheng, W. Liang, M. Hada, M. Ehara, K. Toyota, R. Fukuda, J. Hasegawa, M. Ishida, T. Nakajima, Y. Honda, O. Kitao, H. Nakai, T. Vreven, K. Throssell, J.A. Jr, J.E. Montgomery, F. Peralta, M.J. Ogliaro, J. J. Bearpark, E.N. Heyd, K.N. Brothers, V.N. Kudin, T.A. Staroverov, R. Keith, J. Kobayashi, K. Normand, A.P. Raghavachari, J.C. Rendell, S.S. Burant, J. Iyengar, M. Tomasi, J.M. Cossi, M. Millam, C. Klene, R. Adamo, J.W. Cammi, R.L. Ochterski, K. Martin, O. Morokuma, J.B. Farkas, D.J.F. Foresman, Gaussian 16, Revision C.01, Gaussian Inc., Wallingford CT, 2016.
[32] DTU Computing Center, Technical University of Denmark, 2021. https://www.hpc.dtu.dk.
[33] T. Bruhn, A. Schaumlöffel, Y. Hemberger, G. Pecitelli, SpecDis version 1.71, Berlin, Germany, 2017. https://specdis-software.jimdo.com.
[34] T. Bruhn, A. Schaumlöffel, Y. Hemberger, G. Bringmann, SpecDis: quantifying the comparison of calculated and experimental electronic circular dichroism spectra, Chirality 25 (2013) 243–249.
[35] B.G. Szczepankiewicz, G. Liu, P.J. Hajduk, C. Abad-Zapatero, Z. Pei, Z. Xin, T. H. Lubben, J.M. Trevillyan, M.A. Stashko, S.J. Ballaron, H. Liang, F. Huang, C. W. Hutchins, S.W. Fesik, M.R. Jirousek, Discovery of a potent, selective protein tyrosine phosphatase 1B inhibitor using a linked-fragment strategy, J. Am. Chem. Soc. 125 (14) (2003) 4087–4096.
[36] C. Wiesmann, K.J. Barr, J. Kung, J. Zhu, D.A. Erlanson, W. Shen, B.J. Fahr, M. Zhong, L. Taylor, M. Randal, R.S. McDowell, S.K. Hansen, Allosteric inhibition of protein tyrosine phosphatase 1B, Nat. Struct. Mol. Biol. 11 (2004) 730–737.
[37] K.D. Croft, E.L. Ghisalberti, P.R. Jefferies, D.G. Marshall, C.L. Raston, A.H. White, The chemistry of *Eremophila* spp. XII* a new decipiene diterpene, Aust. J. Chem. 33 (1980) 1529–1536.
[38] A.G. Costa, N.C. Yoshida, W.S. Garcez, R.T. Perdomo, M.d.F.C. Matos, F.R. Garcez, Metabolomics approach expands the classification of *Propolis* samples from midwest Brazil, J. Nat. Prod. 83 (2) (2020) 333–343.
[39] P. Forgo, I. Zupkó, J. Molnár, A. Vasas, G. Dombi, J. Hohmann, Bioactivity-guided isolation of antiproliferative compounds from *Centaurea jacea* L, Fitoterapia 83 (5) (2012) 921–925.
[40] J.E. Miranda-Nuñez, A. Zamilpa-Alvarez, A. Fortis-Barrera, F.J. Alarcon-Aguilar, H. Loza-Rodriguez, L.E. Gomez-Quiroz, S. Salas-Silva, M. Flores-Cruz, M.A. Zavala-Sanchez, G. Blancas-Flores, GLUT4 translocation in C2C12 myoblasts and primary mouse hepatocytes by an antihyperglycemic flavone from *Tillandsia usneoides*, Phytomedicine 89 (2021), 153622.
[41] C. Long, P. Sauleau, B. David, C. Lavaud, V. Cassabois, F. Ausseil, G. Massiot, Bioactive flavonoids of *Tanacetum parthenium* revisited, Phytochemistry 64 (2) (2003) 567–569.
[42] B.K. Datta, M.A. Rashid, J.K. Kundu, A.S. Rouf, S.D. Sarker, S.K. Datta, Isolation and structure elucidation of viscoazucine, a novel sesquiterpene from *Polygonum viscosum*, Pharmazie 56 (2001) 578–579.
[43] L.H. Mai, G.G. Chabot, P. Grellier, L. Quentin, V. Dumontet, C. Poulain, L. S. Espindola, S. Michel, H.T.B. Vo, B. Deguin, R. Grougnet, Antivascular and anti-parasite activities of natural and hemisynthetic flavonoids from New Caledonian *Gardenia* species (Rubiaceae), Eur. J. Med. Chem. 93 (2015) 93–100.
[44] R. Li, L. Song, F. He, W. Zhang, Q. Wang, X. Fan, H. Zhang, Y. Duan, K. Wang, A preparation method of myricetin, C.N. Patent, CN109020938A, 2018.
[45] O. Gericke, N.L. Hansen, G.B. Pedersen, L. Kjaerulff, D. Luo, D. Staerk, B.L. Møller, I. Pateraki, A.M. Heskes, Nerylneryl diphosphate is the precursor of serrulatane, viscidane and cembrane-type diterpenoids in *Eremophila* species, BMC Plant Biol. 20 (2020) 91.
[46] E.L. Ghisalberti, The chemistry of unusual terpenoids from the genus *Eremophila*, Stud. Nat. Prod. Chem. 15 (1995) 225–287.
[47] E.L. Ghisalberti, P.R. Jefferies, G.M. Proudfoot, The chemistry of *Eremophila* spp. XV. New acyclic diterpenes from *Eremophila* spp, Aust. J. Chem. 34 (1981) 1491–1499.
[48] Y.J. Hong, D.J. Tantillo, Branching out from bisabolyl cation: Unifying mechanistic pathways to barbatene, bazzanene, chamigrene, chamipinene, cumacrene, cuprenene, dunniene, isobazznene, iso-γ-bisabolene, isochamigrene, laurene, microbiotene, sesquithujene, sesquisabinene, thujopsene, trichodiene, and widdradiene sesquiterpenes, J. Am. Chem. Soc 136 (2014) 2450–2463.
[49] Y.J. Hong, D.J. Tantillo, How cyclobutanes are assembled in nature-insights from quantum chemistry, Chem. Soc. Rev. 43 (2014) 5042–5050.
[50] T. Bach, J.P. Hehn, Photochemical reactions as key steps in natural product synthesis, Angew. Chem. Int. Ed. 50 (5) (2011) 1000–1045.
[51] K.D. Croft, E.L. Ghisalberti, P.R. Jefferies, A.D. Stuart, The absolute configuration of the dicipiene diterpenoids, Tetrahedron 37 (1981) 383–387.
[52] C.S. Jamieson, M. Ohashi, F. Liu, Y.i. Tang, K.N. Houk, The expanding world of biosynthetic pericyclases: cooperation of experiment and theory for discovery, Nat. Prod. Rep. 36 (5) (2019) 698–713.
[53] M.J. Byrne, N.R. Lees, L.C. Han, M.W. van der Kamp, A.J. Mulholland, J.E. M. Stach, C.L. Willis, P.R. Race, The catalytic mechanism of a natural Diels-Alderase revealed in molecular detail, J. Am. Chem. Soc 138 (2016) 6095–6098.
[54] H. Wang, Y. Zou, M. Li, Z. Tang, J. Wang, Z. Tian, N. Strassner, Q. Yang, Q. Zheng, Y. Guo, W. Liu, L. Pan, K.N. Houk, A cyclase that catalyses competing 2 + 2 and 4 + 2 cycloadditions, Nat. Chem. 15 (2023) 177–184.
[55] A. Sancar, Structure and function of a DNA photolyase, Biochemistry 33 (1994) 2–9.
[56] D.B. Abdjul, H. Yamazaki, W. Maarisit, H. Rotinsulu, D.S. Wewengkang, D. A. Sumilat, M.M. Kapojos, F. Losung, K. Ukai, M. Namikoshi, Oleanane triterpenes with protein tyrosine phosphatase 1B inhibitory activity from aerial parts of *Lantana camara* collected in Indonesia and Japan, Phytochemistry 144 (2017) 106–112.
[57] Y. Zhao, O. Gericke, T. Li, L. Kjaerulff, K.T. Kongstad, A.M. Heskes, B.L. Møller, F. S. Jørgensen, H. Venter, S. Coriani, S.J. Semple, D. Staerk, Polypharmacology-labelled molecular networking: An analytical technology workflow for accelerated identification of multiple bioactive constituents in complex extracts, Anal. Chem. 95 (2023) 4381–4389.
[58] S.C.L. Kamerlin, R. Rucker, S. Boresch, A targeted molecular dynamics study of WPD loop movement in PTP1B, Biochem. Biophys. Res. Commun. 345 (3) (2006) 1161–1166.
[59] M.I. Campos-Almazán, A. Hernández-Campos, R. Castillo, E. Sierra-Campos, M. Valdez-Solana, C. Avitia-Domínguez, A. Téllez-Valencia, Computational methods in cooperation with experimental approaches to design protein tyrosine phosphatase 1B inhibitors in type 2 diabetes drug design: A review of the achievements of this century, Pharmaceuticals 15 (2022) 866.
[60] J.-F. Wang, K. Gong, D.-Q. Wei, Y.-X. Li, K.-C. Chou, Molecular dynamics studies on the interactions of PTP1B with inhibitors: from the first phosphate-binding site to the second one, Protein Eng. Des. Sel. 22 (2009) 349–355.